Monthly Notices
of the
ROYAL ASTRONOMICAL SOCIETY

MNRAS **524,** 1651–1667 (2023)
Advance Access publication 2023 June 28

https://doi.org/10.1093/mnras/stad1935

First test of the consistency relation for the large-scale structure using the anisotropic three-point correlation function of BOSS DR12 galaxies

Naonori S. Sugiyama,[1]★ Daisuke Yamauchi,[2] Tsutomu Kobayashi,[3] Tomohiro Fujita,[4,5] Shun Arai,[6] Shin'ichi Hirano,[7] Shun Saito,[8,9] Florian Beutler[10] and Hee-Jong Seo[11,12,13]

[1] *National Astronomical Observatory of Japan, Mitaka, 181-8588 Tokyo, Japan*
[2] *Department of Physics, Faculty of Science, Okayama University of Science, 1-1 Ridaicho, 700-0005 Okayama, Japan*
[3] *Department of Physics, Rikkyo University, Toshima, 171-8501 Tokyo, Japan*
[4] *Waseda Institute for Advanced Study, Shinjuku, 169-8050 Tokyo, Japan*
[5] *Research Center for the Early Universe, The University of Tokyo, Bunkyo, 113-0033 Tokyo, Japan*
[6] *Kobayashi-Maskawa Institute, Nagoya University, 464-8602 Nagoya, Japan*
[7] *Oyama National College of Technology, 323-0806 Oyama, Japan*
[8] *Institute for Multi-messenger Astrophysics and Cosmology, Department of Physics, Missouri University of Science and Technology, 1315 N. Pine St., Rolla, MO 65409, USA*
[9] *Kavli Institute for the Physics and Mathematics of the Universe (WPI), Todai Institutes for Advanced Study, The University of Tokyo, 277-8582 Chiba, Japan*
[10] *Institute for Astronomy, University of Edinburgh, Royal Observatory, Blackford Hill, Edinburgh EH9 3HJ, UK*
[11] *Department of Physics and Astronomy, Ohio University, Clippinger Labs, Athens, OH 45701, USA*
[12] *Physics Division, Lawrence Berkeley National Laboratory, 1 Cyclotron Road, Berkeley, CA 94720, USA*
[13] *Berkeley Center for Cosmological Physics, Department of Physics, University of California, Berkeley, CA 94720, USA*

Accepted 2023 June 23. Received 2023 June 23; in original form 2023 May 4

ABSTRACT

We present, for the first time, an observational test of the consistency relation for the large-scale structure (LSS) of the Universe through a joint analysis of the anisotropic two- and three-point correlation functions (2PCF and 3PCF) of galaxies. We parameterize the breakdown of the LSS consistency relation in the squeezed limit by $E_{\rm s}$, which represents the ratio of the coefficients of the shift terms in the second-order density and velocity fluctuations. $E_{\rm s} \neq 1$ is a sufficient condition under which the LSS consistency relation is violated. A novel aspect of this work is that we constrain $E_{\rm s}$ by obtaining information about the non-linear velocity field from the quadrupole component of the 3PCF without taking the squeezed limit. Using the galaxy catalogues in the Baryon Oscillation Spectroscopic Survey (BOSS) Data Release 12, we obtain $E_{\rm s} = -0.92^{+3.13}_{-3.26}$, indicating that there is no violation of the LSS consistency relation in our analysis within the statistical errors. Our parameterization is general enough that our constraint can be applied to a wide range of theories, such as multicomponent fluids, modified gravity theories, and their associated galaxy bias effects. Our analysis opens a new observational window to test the fundamental physics using the anisotropic higher-order correlation functions of galaxy clustering.

Key words: large-scale structure of Universe – dark matter – cosmology: observations – cosmology: theory.

1 INTRODUCTION

The consistency relation of multipoint statistics in cosmology is a relation that non-perturbatively relates an n-point statistic of cosmic fluctuations to an $(n-1)$-point statistic. This relation holds in the limit that one of the $n \geq 3$ wavenumbers is much smaller than the others, the so-called *squeezed limit*. Originally proposed for single-field inflationary models (Maldacena 2003; Creminelli & Zaldarriaga 2004), a similar consistency relation was later invented in the large-scale structure (LSS) of the Universe (Creminelli et al. 2013; Kehagias & Riotto 2013; Peloso & Pietroni 2013).

The LSS consistency relation is due to the fact that the equations for cosmic fluctuations are invariant under the Galilean transformation (Scoccimarro & Frieman 1996; Creminelli et al. 2013). In particular, the Galilean transformation eliminates the large-scale flow of matter at equal times, so that all higher-order non-linear contributions beyond the leading order in perturbation theory are cancelled out when computing n-point statistics. This behaviour is called the equal-time consistency relation or infrared (IR) cancellation (Jain & Bertschinger 1996; Scoccimarro & Frieman 1996; Blas, Garny & Konstandin 2013; Kehagias & Riotto 2013; Peloso & Pietroni 2013; Sugiyama & Futamase 2013; Sugiyama & Spergel 2014; Blas et al. 2016; Lewandowski & Senatore 2017). On the other hand, various conditions have been proposed to violate this consistency relation, such as multicomponent fluids (Tseliakhovich & Hirata 2010; Yoo, Dalal & Seljak 2011; Bernardeau, Van de Rijt & Vernizzi 2012, 2013; Creminelli et al. 2014b; Peloso & Pietroni 2014; Lewandowski, Perko & Senatore 2015; Slepian & Eisenstein 2017), primordial non-Gaussianity (Berezhiani & Khoury 2014; Valageas, Taruya &

★ E-mail: nao.s.sugiyama@gmail.com

Published by Oxford University Press on behalf of Royal Astronomical Society

Nishimichi 2017; Esposito, Hui & Scoccimarro 2019; Goldstein et al. 2022), and violation of the equivalence principle (Creminelli et al. 2014a; Inomata, Lee & Hu 2023). It is therefore fundamental to test whether our Universe has a simple structure that satisfies the LSS consistency relation.

Crisostomi, Lewandowski & Vernizzi (2020) and Lewandowski (2020) pointed out that the Degenerate Higher-Order Scalar-Tensor (DHOST) theories (for reviews, see Kobayashi 2019; Langlois 2019), a type of modified gravity, also violate the LSS consistency relation. The reason is that when the second-order dark matter density fluctuations are decomposed into two independent components, the shift term and the tidal force term,[1] DHOST theories change both terms from the values of general relativity (GR; Hirano et al. 2018). On the other hand, Horndeski theories (Horndeski 1974; Deffayet et al. 2011; Kobayashi, Yamaguchi & Yokoyama 2011), a subclass of DHOST theories, change only the tidal term from GR, leaving the shift term unchanged (Bernardeau & Brax 2011; Bartolo et al. 2013; Takushima, Terukina & Yamamoto 2014; Bellini, Jimenez & Verde 2015; Burrage, Dombrowski & Saadeh 2019). Focusing on the LSS consistency relation is equivalent to extracting only the shift term, which is dominant in the squeezed limit, from the dark matter density fluctuations. Therefore, DHOST theories with the modified shift term violate the LSS consistency relation. In other words, the structure of DHOST theories resembles the structure of multicomponent fluids, and the Galilean transformation cannot eliminate the relative velocities of a scalar field and dark matter on large scales, thus violating the LSS consistency relation.

However, observables that trace the LSS consistency relation are not straightforwardly constructed. For example, Crisostomi et al. (2020) pointed out in Section V that taking the squeezed limit of the galaxy bispectrum does not directly test the violation of the LSS consistency relation in DHOST theories. The reason is that the bispectrum, which depends on the three wavenumbers k_1, k_2, and k_3, is symmetric with respect to these variables; taking the squeezed limit cancels out any change in the shift term that violates the consistency relation. Therefore, the authors proposed to measure the cross-bispectrum with other cosmic fluctuations, such as gravitational lensing effects, or to measure the trispectrum of galaxies, so that the effects of DHOST theories are not cancelled when the squeezed limit is taken.

Recent rapid developments in the analysis of galaxy three-point statistics, i.e. bispectra and three-point correlation functions (3PCFs), have allowed us to test the consistency relation. In principle, the three-point statistics (not restricted to the squeezed limit) are sensitive to the coefficient of the shift term of the galaxy density fluctuation. However, a critical problem remains to be solved: Most previous studies deal only with the isotropic, i.e. *monopole*, component of the three-point statistics (Gil-Marín et al. 2017; Slepian et al. 2017; Pearson & Samushia 2018; Sugiyama et al. 2019; d'Amico et al. 2020; Cabass et al. 2022a, b; D'Amico et al. 2022a; Philcox & Ivanov 2022), and these analyses cannot efficiently constrain the coefficient of the non-linear density field shift term. The reason is that in the monopole-only analysis, the coefficient of the density fluctuation shift term degenerates with the parameter σ_8, which represents the amplitude of the dark matter fluctuations (Sugiyama et al. 2023).

Yamauchi & Sugiyama (2022) pointed out that the use of non-linear velocity fields in addition to non-linear density fields is helpful in studying non-linear gravitational effects. The non-linear velocity field can be directly constrained by analysing the anisotropic, e.g. *quadrupole*, component of the galaxy three-point statistics. Although the analysis of the anisotropic component of the galaxy three-point statistic is much less mature than the monopole-only analysis, some of us have successfully initiated such efforts. For example, Sugiyama et al. (2019) proposed a new basis for measuring the anisotropic bispectra and reported the significant detection of the anisotropic component from the galaxy catalogue from the Baryon Oscillation Spectroscopic Survey Data Release 12 (BOSS DR12; Eisenstein et al. 2011; Bolton et al. 2012; Dawson et al. 2013; Alam et al. 2015). Sugiyama et al. (2021) analysed the anisotropic component of Baryon Acoustic Oscillations (BAOs; Peebles & Yu 1970; Sunyaev & Zeldovich 1970) using the anisotropic 2PCF and 3PCF on MultiDark-Patchy mock simulations (Patchy mock; Kitaura et al. 2016; Klypin et al. 2016) that reproduce the BOSS DR12 galaxy data. D'Amico et al. (2022b) performed the first joint analysis of the monopole and quadrupole components of the power and bispectra measured from BOSS DR12 and constrained the standard cosmological parameters in the context of Λ cold dark matter (ΛCDM). Ivanov et al. (2023) presented the results of an anisotropic bispectrum analysis including quadrupole and hexadecapole components measured from the BOSS DR12 data. In particular, Sugiyama et al. (2023) applied the analysis method of Sugiyama et al. (2021) to the BOSS galaxy data, based on the idea proposed by Yamauchi & Sugiyama (2022) to constrain the effects of gravitational non-linearities arising from DHOST theories in a σ_8-independent manner.

The aim of this paper is to present, for the first time, an observational test of the LSS consistency relation in galaxy clustering in BOSS. We mostly follow the analysis method used in Sugiyama et al. (2023; hereafter referred to as S23). In order to ensure that the obtained results are applicable to as many different situations as possible, we propose a general parameterization that includes modified gravity theories, multicomponent fluids, and galaxy bias effects in the description of non-linear density and velocity fields, thus constraining the LSS consistency relation in a broad framework. Conversely, when a violation of the LSS consistency relation is detected, a more specific model is required to provide a physical interpretation of the violation. We also present some specific examples of models that are and are not part of the parameterization framework used in this paper.

Our analysis uses a flat ΛCDM model as the fiducial cosmological model with the following parameters: matter density $\Omega_{\rm m0} = 0.31$, Hubble constant $h \equiv H_0/(100\,{\rm km\,s^{-1}\,Mpc^{-1}}) = 0.676$, baryon density $\Omega_{\rm b0}h^2 = 0.022$, and spectral tilt $n_{\rm s} = 0.97$, which are the same as those used in the final cosmological analysis in the BOSS project (Alam et al. 2017) and close to the best-fitting values given by Planck2018 (Aghanim et al. 2020). In addition, we adopt a value for the total neutrino mass of $\sum m_\nu = 0.06\,{\rm eV}$, which is close to the minimum allowed by neutrino oscillation experiments. We use the following publicly available libraries to perform theoretical calculations, measure 2PCF and 3PCF from galaxy data, and estimate parameter likelihoods using Markov chain Monte Carlo (MCMC) methods: MONTE PYTHON (Brinckmann & Lesgourgues 2019), CLASS (Blas, Lesgourgues & Tram 2011), CUBA (Hahn 2005), FFTW (Frigo & Johnson 2005), and FFTLOG (Hamilton 2000).

---

[1] The scale dependence of the second-order density fluctuation of dark matter is generally decomposed into the growth, shift, and tidal terms (Schmittfull, Baldauf & Seljak 2015). However, due to the condition that the ensemble average (infinite space integral) of the dark matter density fluctuation is zero, the coefficients of the three terms are related, and there are only two independent components. This relation is known to break down when galaxy bias effects are taken into account, in which case these three independent components must be considered (e.g. Desjacques, Jeong & Schmidt 2018).

The structure of this paper is as follows. Section 2 describes the theoretical model used in this paper and the parameters to be constrained; Section 3 briefly summarizes the data analysis methods; Section 4 presents the results of the parameter constraints; Section 5 concludes the paper; Appendix A summarizes the results of other parameters not presented in the main text.

2 THEORETICAL BACKGROUND

2.1 Parameterization of non-linear fluctuations

In this paper, we consider non-linear effects up to the second order in perturbation theory since, in Section 2.4, we compute the 2PCF and 3PCF models based on the tree-level, taking into account non-linear damping of the BAO. In Fourier space, the redshift-space density fluctuations of galaxies are expressed as (e.g, Bernardeau et al. 2002)

$$\begin{aligned}\delta_1(\boldsymbol{k}) &= Z_1(\boldsymbol{k})\delta_{\mathrm{m},1}(\boldsymbol{k}),\\ \delta_2(\boldsymbol{k}) &= \int\frac{d^3p_1}{(2\pi)^3}\int\frac{d^3p_2}{(2\pi)^3}\delta_{\mathrm{D}}(\boldsymbol{k}-\boldsymbol{p}_1-\boldsymbol{p}_2)\\ &\quad\times Z_2(\boldsymbol{p}_1,\boldsymbol{p}_2)\delta_{\mathrm{m},1}(\boldsymbol{p}_1)\delta_{\mathrm{m},1}(\boldsymbol{p}_2),\end{aligned} \tag{1}$$

where the numbers in the subscripts mean that the solution is of the first and second order in perturbation theory. The δ_{m} appearing on the right-hand side represents the dark matter density fluctuation.

The first and second-order kernel functions Z_1 and Z_2 are given by (Kaiser 1987; Scoccimarro, Couchman & Frieman 1999)

$$\begin{aligned}Z_1(\boldsymbol{k}) &= b_1 + f(\hat{k}\cdot\hat{n})^2,\\ Z_2(\boldsymbol{k}_1,\boldsymbol{k}_2) &= F_2(\boldsymbol{k}_1,\boldsymbol{k}_2) + f(\hat{k}\cdot\hat{n})^2G_2(\boldsymbol{k}_1,\boldsymbol{k}_2)\\ &\quad+\frac{f(\boldsymbol{k}\cdot\hat{n})}{2}\left[\frac{(\hat{k}_1\cdot\hat{n})}{k_1}Z_1(\boldsymbol{k}_2)+\frac{(\hat{k}_2\cdot\hat{n})}{k_2}Z_1(\boldsymbol{k}_1)\right],\end{aligned} \tag{2}$$

where b_1 is the linear bias parameter, f is the linear growth rate function, $\hat{n}$ is the unit vector that indicates the direction of the line of sight, and $\boldsymbol{k} = \boldsymbol{k}_1 + \boldsymbol{k}_2$.

The kernel functions F_2 and G_2, which represent the second-order non-linearity of the galaxy density fluctuation and the divergence of the galaxy velocity field, are decomposed into monopole, dipole, and quadrupole via the angle between $\boldsymbol{k}_1$ and $\boldsymbol{k}_2$ and are called the growth, shift, and tidal terms, respectively (Schmittfull et al. 2015). We then introduce the following parameterization for each coefficient of these terms:

$$\begin{aligned}F_2(\boldsymbol{k}_1,\boldsymbol{k}_2) &= b_1\left[F_{\mathrm{g}} + F_{\mathrm{s}}\,S(\boldsymbol{k}_1,\boldsymbol{k}_2) + F_{\mathrm{t}}\,T(\boldsymbol{k}_1,\boldsymbol{k}_2)\right],\\ f\,G_2(\boldsymbol{k}_1,\boldsymbol{k}_2) &= f\left[G_{\mathrm{g}} + G_{\mathrm{s}}\,S(\boldsymbol{k}_1,\boldsymbol{k}_2) + G_{\mathrm{t}}\,T(\boldsymbol{k}_1,\boldsymbol{k}_2)\right],\end{aligned} \tag{3}$$

where the subscripts ‘g’, ‘s’, and ‘t’ stand for ‘growth’, ‘shift’, and ‘tidal’, respectively. The scale-dependent functions characterizing the shift and tidal terms are given by

$$\begin{aligned}S(\boldsymbol{k}_1,\boldsymbol{k}_2) &= \frac{1}{2}(\hat{k}_1\cdot\hat{k}_2)\left(\frac{k_1}{k_2}+\frac{k_2}{k_1}\right),\\ T(\boldsymbol{k}_1,\boldsymbol{k}_2) &= (\hat{k}_1\cdot\hat{k}_2)^2 - \frac{1}{3}.\end{aligned} \tag{4}$$

Since the linear and non-linear fluctuations are proportional to σ_8 and σ_8^2, respectively, the parameters we focus on will appear in a degenerate form with σ_8, such as $(b_1\sigma_8)$, $(f\sigma_8)$, $(F_{\mathrm{g}}\sigma_8)$, $(F_{\mathrm{s}}\sigma_8)$, $(F_{\mathrm{t}}\sigma_8)$, $(G_{\mathrm{g}}\sigma_8)$, $(G_{\mathrm{s}}\sigma_8)$, and $(G_{\mathrm{t}}\sigma_8)$. Therefore, we introduce the following parameter to remove the dependence of σ_8 and express the violation of the LSS consistency relation (Yamauchi & Sugiyama 2022; Sugiyama et al. 2023):

$$E_{\mathrm{s}} \equiv \frac{(G_{\mathrm{s}}\sigma_8)}{(F_{\mathrm{s}}\sigma_8)}. \tag{5}$$

This E_{s} parameter satisfies $E_{\mathrm{s}} = 1$ when $F_{\mathrm{s}} = G_{\mathrm{s}}$. For example, in GR, $E_{\mathrm{s}} = 1$ since $F_{\mathrm{s}} = G_{\mathrm{s}} = 1$. On the other hand, $E_{\mathrm{s}} \neq 1$ is satisfied if either F_{s} or G_{s} or both are different from 1, while keeping $F_{\mathrm{s}} \neq G_{\mathrm{s}}$. This means that the condition $E_{\mathrm{s}} \neq 1$ indicates a violation of the LSS consistency relation. This is because taking the squeezed limit of the bispectrum corresponds to the operation of extracting only these shift terms. Note that $E_{\mathrm{s}} \neq 1$ is a sufficient condition for proving the violation of the LSS consistency relation, not a necessary condition, since a particular theory may satisfy $F_{\mathrm{s}} = G_{\mathrm{s}} \neq 1$.

2.2 Consistency relation for the LSS

In this subsection, we show that the E_{s} parameter is useful for testing the violation of the LSS consistency relation. To do this, we focus on the bispectrum produced by the galaxy density fluctuations at three different redshifts, i.e.

$$\begin{aligned}&\langle\delta(\boldsymbol{k}_1;z_1)\delta(\boldsymbol{k}_2;z_2)\delta(\boldsymbol{k}_3;z_3)\rangle\\ &= (2\pi)^3\delta_{\mathrm{D}}\left(\boldsymbol{k}_1+\boldsymbol{k}_2+\boldsymbol{k}_3\right)B(\boldsymbol{k}_1,\boldsymbol{k}_2;z_1,z_2,z_3),\end{aligned} \tag{6}$$

and take its squeezed limit $k_1 \to 0$. Note that this subsection is the only one in this paper that explicitly denotes the redshift dependence in the functions.

Satisfying the LSS consistency relation means that when taking the squeezed limit of the n-point statistics, the effect is described only by the contribution of the dark matter displacement vector evaluated at the origin. In real space, the linear displacement vector is $\Psi_{\mathrm{m},1}(\boldsymbol{k}) = (i\boldsymbol{k}/k^2)\delta_{\mathrm{m},1}(\boldsymbol{k})$, and in redshift space, it is computed by a linear transformation as

$$\Psi_{\mathrm{s},1}(\boldsymbol{k};z) = \boldsymbol{R}(z)\cdot\Psi_{\mathrm{m},1}(\boldsymbol{k};z), \tag{7}$$

where the transformation matrix $\boldsymbol{R}$ is given by (Matsubara 2008)

$$[\boldsymbol{R}(z)]_{ij} = \boldsymbol{I}_{ij} + f(z)\,\hat{n}_i\hat{n}_j, \tag{8}$$

where $\boldsymbol{I}$ is the 3D identity matrix, and $i, j = 1, 2, 3$.

For simplicity, we consider only the tree-level bispectrum. From equation (1), the non-linear contribution from a wavenumber k_1 or k_2 sufficiently smaller than the wavenumber k of interest is given by the limit $k \gg k_1 \to 0$ or $k \gg k_2 \to 0$ and can be written as follows:

$$\delta_2(\boldsymbol{k};z) \to 2\delta_{\mathrm{m},1}(\boldsymbol{k};z)\int\frac{d^3p}{(2\pi)}Z_2(\boldsymbol{p},\boldsymbol{k};z)|_{p\to0}\delta_{\mathrm{m},1}(\boldsymbol{p};z). \tag{9}$$

If $F_{\mathrm{s}} = G_{\mathrm{s}} = 1$, then

$$\delta_2(\boldsymbol{k};z) \to (-i\boldsymbol{k}\cdot\overline{\Psi}_{\mathrm{s},1}(z))\delta_1(\boldsymbol{k};z), \tag{10}$$

where

$$\overline{\Psi}_{\mathrm{s},1}(z) = \int\frac{d^3p}{(2\pi)^3}\Psi_{\mathrm{s},1}(\boldsymbol{p},z). \tag{11}$$

The above equation represents the inverse Fourier transform, and $\overline{\Psi}_{\mathrm{s},1}$ is the displacement vector at the origin $\boldsymbol{x} = \boldsymbol{0}$ and is independent of positions. In other words, $\overline{\Psi}_{\mathrm{s},1}$ can be interpreted as a large-scale flow of dark matter through the entire observation region.

Taking the squeezed limit $k_1 \to 0$ in the bispectrum of equation (6), $\delta(\boldsymbol{k}_1;z_1)$ is only correlated with $\overline{\Psi}_{\mathrm{s},1}(z_2)$ or $\overline{\Psi}_{\mathrm{s},1}(z_3)$. Therefore,

$$\begin{aligned}&\langle\delta(\boldsymbol{k}_1;z_1)\delta(\boldsymbol{k}_2;z_2)\delta(\boldsymbol{k}_3;z_3)\rangle\\ &\xrightarrow[k_1\to0]{}\left\langle\left(-i\boldsymbol{k}_2\cdot\left(\overline{\Psi}_{\mathrm{s},1}(z_2)-\overline{\Psi}_{\mathrm{s},1}(z_3)\right)\right)\delta_1(\boldsymbol{k}_1;z_1)\right\rangle\\ &\times\ \langle\delta_1(\boldsymbol{k}_2;z_2)\delta_1(\boldsymbol{k}_3;z_3)\rangle,\end{aligned} \tag{12}$$

leading to the LSS consistency relation

$$\begin{aligned} & B(\boldsymbol{k}_1, \boldsymbol{k}_2; z_1, z_2, z_3) \\ \xrightarrow[k_1\to 0]{} \; & \tilde{Z}_1(\boldsymbol{k}_1; z_1)\tilde{Z}_1(\boldsymbol{k}_2; z_2)\tilde{Z}_1(\boldsymbol{k}_2; z_3)\tilde{P}_{\rm lin}(k_1)\tilde{P}_{\rm lin}(k_2) \\ \times \; & \left\{\sigma_8(z_3)\frac{\boldsymbol{k}_1\cdot\boldsymbol{R}(z_3)\cdot\boldsymbol{k}_2}{k_1^2} - \sigma_8(z_2)\frac{\boldsymbol{k}_1\cdot\boldsymbol{R}(z_2)\cdot\boldsymbol{k}_2}{k_1^2}\right\}, \end{aligned} \tag{13}$$

where

$$\langle \delta_{{\rm m},1}(\boldsymbol{k}; z)\delta_{{\rm m},1}(\boldsymbol{k}'; z)\rangle = (2\pi)^3\delta_{\rm D}(\boldsymbol{k}+\boldsymbol{k}')P_{\rm lin}(k; z) \tag{14}$$

gives the linear matter power spectrum, and $\tilde{P}_{\rm lin}$ and $\tilde{Z}_1$ are defined as $\tilde{P}_{\rm lin}(k) = P_{\rm lin}(k; z)/\sigma_8^2(z)$ and $\tilde{Z}_1(\boldsymbol{k}; z) = Z_1(\boldsymbol{k}; z)\sigma_8(z)$, respectively.

On the other hand, if $F_{\rm s} \neq 1$ and $G_{\rm s} \neq 1$ are allowed, the tree-level bispectrum in the squeezed limit can be calculated as

$$\begin{aligned} & B(\boldsymbol{k}_1, \boldsymbol{k}_2; z_1, z_2, z_3) \\ \xrightarrow[k_1\to 0]{} \; & \tilde{Z}_1(\boldsymbol{k}_1; z_1)\tilde{Z}_1(\boldsymbol{k}_2; z_2)\tilde{Z}_1(\boldsymbol{k}_2; z_3)\tilde{P}_{\rm lin}(k_1)\tilde{P}_{\rm lin}(k_2) \\ \times \; & \left\{\left(\frac{\boldsymbol{k}_1\cdot\boldsymbol{k}_2}{k_1^2}\right)[(F_{\rm s}\sigma_8)(z_3) - (F_{\rm s}\sigma_8)(z_2)]\right. \\ + \; & \left.\left(\frac{(\boldsymbol{k}_1\cdot\hat{n})(\boldsymbol{k}_2\cdot\hat{n})}{k_1^2}\right)[(f\sigma_8)(z_3) - (f\sigma_8)(z_2)]\right\} \\ + \; & \left(\hat{k}_2\cdot\hat{n}\right)^2 \tilde{Z}_1(\boldsymbol{k}_1; z_1)\left(\frac{\boldsymbol{k}_1\cdot\boldsymbol{k}_2}{k_1^2}\right)\tilde{P}_{\rm lin}(k_1)\tilde{P}_{\rm lin}(k_2) \\ \times \; & \Big\{(f\sigma_8)(z_3)(F_{\rm s}\sigma_8)(z_3)\left(E_{\rm s}(z_3)-1\right)\tilde{Z}_1(\boldsymbol{k}_2; z_2) \\ - \; & (f\sigma_8)(z_2)(F_{\rm s}\sigma_8)(z_2)\left(E_{\rm s}(z_2)-1\right)\tilde{Z}_1(\boldsymbol{k}_2; z_3)\Big\}. \end{aligned} \tag{15}$$

Substituting $F_{\rm s} = E_{\rm s} = 1$ into the above equation gives equation (13). In other words, the LSS consistency relation is broken when $F_{\rm s} \neq 1$ or $E_{\rm s} \neq 1$. Also, as expected, $F_{\rm s}$ only appears in the form $(F_{\rm s}\sigma_8)$, indicating that the $E_{\rm s}$ parameter, which does not depend on σ_8, is the most appropriate for investigating the breakdown of the LSS consistency relation. However, since $\sigma_8 > 0$ by definition, $(F_{\rm s}\sigma_8 < 0)$ also implies the breakdown of the LSS consistency relation.

In actual observations, measuring correlators between galaxy density fluctuations at different redshifts is challenging. This is because the galaxy density fields at different redshifts are so far apart in the radial direction that they cannot be correlated. Therefore, it is common to measure the correlators of the galaxy density fields at equal time, so that $z_1 = z_2 = z_3$. In this case, the right-hand side of equation (15) is always zero, because the remaining k_2 and k_3 dependencies are exchangeable when the squeezed limit $k_1 \to 0$ is taken between k_1, k_2, and k_3, on which the bispectrum is symmetrically dependent. This cancellation occurs even if $F_{\rm s}$ and $G_{\rm s}$ are scale-dependent functions with exchange symmetry (see Section 2.3.9 for an example). Therefore, we propose to constrain $(F_{\rm s}\sigma_8)$ and $E_{\rm s}$ directly from the equal-time bispectrum (or 3PCF) without taking the squeezed limit. In this case, we simultaneously vary $(F_{\rm g}\sigma_8)$, $(F_{\rm t}\sigma_8)$, $(G_{\rm g}\sigma_8)$, and $(G_{\rm t}\sigma_8)$ as free parameters so that the results are valid in as general a situation as possible. More details on the physical meaning of these parameters are given in the following subsection.

We will focus only on the results for $E_{\rm s}$ in the main text, but the constraint results for the other non-linear parameters, i.e. $(F_{\rm g}\sigma_8)$, $(F_{\rm s}\sigma_8)$, $(F_{\rm t}\sigma_8)$, $(G_{\rm g}\sigma_8)$, $(G_{\rm s}\sigma_8)$, and $(G_{\rm t}\sigma_8)$, are summarized in Appendix A.

2.3 Specific examples

In this subsection, we discuss specific examples of models that are and are not covered by the parameterization introduced in equation (3).

2.3.1 *ΛCDM*

In the ΛCDM model assuming $f^2 = \Omega_{\rm m}$, the dark matter density and velocity fluctuations give (e.g. Bernardeau et al. 2002)

$$\begin{aligned} F_{\rm g} &= \frac{17}{21}, \quad F_{\rm s} = 1, \quad F_{\rm t} = \frac{2}{7}, \\ G_{\rm g} &= \frac{13}{21}, \quad G_{\rm s} = 1, \quad G_{\rm t} = \frac{4}{7}. \end{aligned} \tag{16}$$

More generally, $f \sim \Omega_{\rm m}^{6/11}$ is a better approximation in a ΛCDM model. Then, the coefficients of the growth and tidal terms are also time-dependent (e.g. Fasiello, Fujita & Vlah 2022). In particular, the following approximate formulae are given in the case where $f = \Omega_{\rm m}^{6/11}$ (Bouchet et al. 1992; Bouchet et al. 1995; Yamauchi, Yokoyama & Tashiro 2017; Yamauchi & Sugiyama 2022):

$$\begin{aligned} F_{\rm g} &= F_{\rm s} - \frac{2}{3}F_{\rm t}, \quad F_{\rm s} = 1, \quad F_{\rm t} = \frac{2}{7}\,\Omega_{\rm m}^{3/572}, \\ G_{\rm g} &= G_{\rm s} - \frac{2}{3}G_{\rm t}, \quad G_{\rm s} = 1, \quad G_{\rm t} = \frac{4}{7}\,\Omega_{\rm m}^{15/1144}. \end{aligned} \tag{17}$$

Note that the growth terms are not independent but are given by the shift and tidal terms. The reason is that the second-order kernel functions satisfy $F_2(\boldsymbol{k}, -\boldsymbol{k}) = 0$ and $G_2(\boldsymbol{k}, -\boldsymbol{k}) = 0$. This condition corresponds to the second-order density fluctuation smoothly approaching zero on large scales, i.e. $\delta_2(\boldsymbol{k} \to 0) \to 0$, which represents the natural behaviour as a non-linear effect.

2.3.2 *Horndeski theories*

Horndeski gravity theories are the most general scalar-tensor theory with second-order equations of motion for metric tensor and scalar fields (Horndeski 1974; Deffayet et al. 2011; Kobayashi et al. 2011). In the Horndeski family of theories, the dark matter second-order density and velocity fields have time-dependent tidal terms, which are found to have a different time evolution than in the ΛCDM case (e.g. Takushima et al. 2014),

$$\begin{aligned} F_{\rm g} &= F_{\rm s} - \frac{2}{3}F_{\rm t}, \quad F_{\rm s} = 1, \quad F_{\rm t} = \frac{2}{7}\lambda_\delta, \\ G_{\rm g} &= G_{\rm s} - \frac{2}{3}G_{\rm t}, \quad G_{\rm s} = 1, \quad G_{\rm t} = \frac{4}{7}\lambda_\theta, \end{aligned} \tag{18}$$

where λ_δ and λ_θ are time-dependent functions, and they are related to each other as

$$\lambda_\theta = \lambda_\delta\left[1 + \frac{1}{2f}\frac{d\ln\lambda_\delta}{d\ln a}\right] \tag{19}$$

with a being the scale factor.

Compared to equation (17), Yamauchi et al. (2017) proposed to test the non-linearity of Horndeski theories by using the parameterization

$$\lambda_\delta = \Omega_{\rm m}^{\xi}. \tag{20}$$

While it is widely used in linear theory to test modified gravity theories by constraining $\gamma = \log_{\Omega_{\rm m}}(f)$, this parameterization is an extension to non-linear effects. The authors also showed that ξ contains new information compared to γ in the test of Horndeski theories by giving a specific model that satisfies $\gamma = 6/11$ and $\xi \neq 3/573$.

2.3.3 DHOST theories

Going beyond Horndeski theories, DHOST theories have been recently discovered (for reviews, Kobayashi 2019; Langlois 2019). Even though DHOST theories have higher-order equations of motion, they reduce in the end to a second-order system thanks to the degeneracy between the kinetic terms of the scalar and metric fields, leading to healthy scalar-tensor theories. In the dark matter second-order density and velocity fields in these theories, in addition to the tidal terms, the shift terms also become time-dependent and deviate from the ΛCDM prediction of 1 (e.g. Hirano et al. 2018),

$$F_{\rm g} = F_{\rm s} - \frac{2}{3}F_{\rm t}, \quad F_{\rm s} = \kappa_\delta, \quad F_{\rm t} = \frac{2}{7}\lambda_\delta,$$
$$G_{\rm g} = G_{\rm s} - \frac{2}{3}G_{\rm t}, \quad G_{\rm s} = \kappa_\theta, \quad G_{\rm t} = \frac{4}{7}\lambda_\theta, \tag{21}$$

where κ_δ and κ_θ are time-dependent functions, and they are related via

$$\kappa_\theta = 2\kappa_\delta\left[1 + \frac{1}{2f}\frac{d\ln\kappa_\delta}{d\ln a}\right] - 1. \tag{22}$$

Yamauchi & Sugiyama (2022) proposed the following parameterization for observationally testing DHOST theories,

$$\frac{f}{\kappa_\delta} = \Omega_{\rm m}^{\xi_f}, \quad \frac{\kappa_\theta}{\kappa_\delta} = \Omega_{\rm m}^{\xi_{\rm s}}, \quad \frac{\lambda_\theta}{\kappa_\delta} = \Omega_{\rm m}^{\xi_{\rm t}}, \tag{23}$$

and pointed out that any non-vanishing value of $\xi_{\rm s}$ can be treated as a clear signal of the existence of a gravity theory beyond Horndeski theories. S23 constrained these index parameters using the BOSS DR12 galaxies and the results are

$$-0.907 < \xi_f < 2.447,$$
$$-1.655 < \xi_{\rm t},$$
$$-0.504 < \xi_{\rm s} \tag{24}$$

at the 95 per cent confidence level. Note that the upper bounds on $\xi_{\rm t}$ and $\xi_{\rm s}$ are not given because $(\lambda_\theta/\kappa_\delta)$ and $(\kappa_\theta/\kappa_\delta)$ are consistent with zero within the 95 per cent error, and $\xi_{\rm t}$ and $\xi_{\rm s}$ can each take infinitely large values as $(\lambda_\theta/\kappa_\delta)$ and $(\kappa_\theta/\kappa_\delta)$ approach zero.

The middle equation in equation (23) corresponds to the $E_{\rm s}$ parameter introduced in equation (5), i.e. $E_{\rm s} = \kappa_\theta/\kappa_\delta$. However, while this paper follows the analysis approach of S23, it is no longer restricted to DHOST theories and assumes a more general situation that includes effects other than those of modified gravity theories. Even if the results of this paper are used to constrain DHOST theories, there are two obvious differences with S23. First, while S23 assumes the standard bias theory given in Section 2.3.8, this paper assumes the existence of more general bias parameters in Section 2.3.10 and varies all non-linear parameters $F_{\rm g}$, $F_{\rm s}$, $F_{\rm t}$, $G_{\rm g}$, $G_{\rm s}$, and $G_{\rm t}$ as free parameters. Secondly, the parameterization given in equation (23) implicitly assumes $E_{\rm s} > 0$, whereas this paper allows negative $E_{\rm s}$.

2.3.4 5D brane-world model

The normal branch of the 5D Dvali–Gabadadze–Porrati brane-world model (nDGP; Dvali, Gabadadze & Porrati 2000), which is a kind of modified gravity theories with extra dimensions, has been well studied. However, since the effects of the extra dimension can be described effectively as a scalar field, this brane-world model can be subsumed into scalar-tensor theories.

The nDGP model is characterized by a non-linear function that modifies the Poisson equation (e.g. Koyama, Taruya & Hiramatsu 2009; Bose & Koyama 2016),

$$\gamma_2(\boldsymbol{k}_1, \boldsymbol{k}_2) \propto \left(1 - \left(\hat{k}_1 \cdot \hat{k}_2\right)^2\right) = \frac{2}{3} - T\left(\boldsymbol{k}_1, \boldsymbol{k}_2\right), \tag{25}$$

varying the tidal term from GR. Once the tidal term is determined, the growth term is also determined by $\gamma_2(\boldsymbol{k}, -\boldsymbol{k}) = 0$. Thus, the nDGP model can be described by a parameterization similar to the Horndeski theories in Section 2.3.2.

2.3.5 f(R) *gravity*

In this subsection, we discuss the Hu–Sawicki model (Hu & Sawicki 2007) of $f(R)$ gravity (see Capozziello & Francaviglia 2008; Sotiriou & Faraoni 2010, for reviews), which is widely used in cosmology. The Hu–Sawicki model predicts non-linear functions that modify the Poisson equation as follows (e.g, Koyama et al. 2009; Bose & Koyama 2016):

$$\gamma_2(\boldsymbol{k}_1, \boldsymbol{k}_2) \propto \left(\frac{k_{12}}{aH}\right)^2 \frac{1}{\Pi(k_{12})\Pi(k_1)\Pi(k_2)},$$
$$\Pi(k) = \left(\frac{k}{a}\right)^2 + \frac{H_0^2\left(\Omega_{\rm m0} - 4a^3\left(\Omega_{\rm m0} - 1\right)\right)^3}{2|f_{R0}|a^9\left(3\Omega_{\rm m0} - 4\right)^2}, \tag{26}$$

where $\boldsymbol{k}_{12} = \boldsymbol{k}_1 + \boldsymbol{k}_2$, H_0 and $\Omega_{\rm m0}$ are the Hubble parameter and the current matter density fraction, respectively, and $|f_{R0}|$ is a free parameter of the theory. Note that in this model, unlike the other models presented in this paper, even linear density fluctuations cannot separate the time dependence from the wavenumber dependence.

The relationship between $f(R)$ gravity and scalar-tensor gravity, and their possible equivalence, has been extensively studied (e.g. Sotiriou 2006). In particular, the gravitational non-linear effects that are the focus of this paper have been discussed in relation to Horndeski theories in Appendix B of Bose & Koyama (2016). However, the gravitational non-linearities obtained from the Hu–Sawicki model differ from those of the Horndeski type discussed in Section 2.3.2. We suspect that this difference is due to the fact that the non-linear effects given in Section 2.3.2 focus only on the terms for which the spatial derivative is most active in the quasi-static approximation, and neglect the terms corresponding to the mass terms of the scalar field, while the $f(R)$ gravity model retains such terms. Since a detailed proof of this is beyond the scope of this paper, we limit ourselves to pointing out that the non-linear effect of the Hu–Sawicki model given by equation (26) does not fit into the parameterization framework used in this paper.

2.3.6 Nearly horizon scales

This paper focuses on the LSS consistency relation in the sub-horizon limit. Thus, even in the GR case, at large scales close to the horizon scale, there are additional correction terms for the non-linear effects given in Section 2.3.1, which are derived in the Newtonian limit. For example, following Tram et al. (2016), a correction term proportional to $(aH/k)^2$ arises for $F_{\rm g}$, $F_{\rm s}$ and $F_{\rm t}$, respectively, and a new scale dependence emerges as follows:

$$\mathcal{K}(\boldsymbol{k}_1, \boldsymbol{k}_2) \propto \left(\frac{aH}{k_{12}}\right)^2\left(\frac{k_1}{k_2} - \frac{k_2}{k_1}\right)^2. \tag{27}$$

Therefore, the parameterization used in this paper is only valid at the sub-horizon scale. See also Creminelli et al. (2013) for a fully relativistic consistency relation. Inomata et al. (2023) also provide a detailed study of squeezed n-point functions in synchronous gauge.

2.3.7 Massive neutrinos

In the remainder of this section, we denote the non-linear parameters for dark matter in a gravity theory described in Sections 2.3.1–2.3.4 as $F^{(\mathrm{m})}_{\mathrm{g,s,t}}$ and $G^{(\mathrm{m})}_{\mathrm{g,s,t}}$ and the additional correction terms for them as $\Delta F^{(\mathrm{m})}_{\mathrm{g,s,t}}$ and $\Delta G^{(\mathrm{m})}_{\mathrm{g,s,t}}$: i.e.

$$F_{\mathrm{g,s,t}} = F^{(\mathrm{m})}_{\mathrm{g,s,t}} + \Delta F_{\mathrm{g,s,t}},$$
$$G_{\mathrm{g,s,t}} = G^{(\mathrm{m})}_{\mathrm{g,s,t}} + \Delta G_{\mathrm{g,s,t}}. \tag{28}$$

Massive neutrinos can modify the second-order kernel functions, in which case the following correction terms are added to the non-linear parameters (Kamalinejad & Slepian 2020):

$$\Delta F_{\mathrm{g}} = \frac{4}{245} f_\nu, \quad \Delta F_{\mathrm{s}} = 0, \quad \Delta F_{\mathrm{t}} = -\frac{6}{245} f_\nu,$$
$$\Delta G_{\mathrm{g}} = -\frac{83}{245} f_\nu, \quad \Delta G_{\mathrm{s}} = -\frac{3}{5} f_\nu, \quad \Delta G_{\mathrm{t}} = -\frac{96}{245} f_\nu, \tag{29}$$

where the neutrino density fraction f_ν is given by

$$f_\nu = \frac{\Omega_\nu}{\Omega_{\mathrm{m}}} \tag{30}$$

with Ω_ν and Ω_{m} being the neutrino and matter energy densities in units of the critical density, respectively. It is important to note that the massive neutrinos do not change the shift term of the density fluctuation but correct the shift term of the velocity fluctuation.

Finally, we estimate the extent to which E_{s} deviates from 1 in the presence of massive neutrinos. The neutrino density fraction is given by (e.g. Takada, Komatsu & Futamase 2006)

$$f_\nu = 0.05 \left(\frac{\sum m_\nu}{0.658\,\mathrm{eV}}\right)\left(\frac{0.14}{\Omega_{\mathrm{m}} h^2}\right). \tag{31}$$

According to current observations, the upper limit for the total neutrino mass is $\sum m_\nu \lesssim 0.1$ eV at 95 per cent confidence level (CL) (e.g. Di Valentino, Gariazzo & Mena 2021). Consequently, substituting $\sum m_\nu = 0.1$ eV into equation (31), the expected value of $E_{\mathrm{s}} - 1 = -(3/5) f_\nu$ is then

$$E_{\mathrm{s}} - 1 = -0.0046 \left(\frac{\sum m_\nu}{0.1\,\mathrm{eV}}\right)\left(\frac{0.14}{\Omega_{\mathrm{m}} h^2}\right). \tag{32}$$

Thus, the impact of the neutrino masses in E_{s} would be minimal, since the 1σ error for E_{s} obtained from the current BOSS data is about 3 in Section 4.2. Put differently, it would be challenging to strongly constrain neutrino masses in the future using only E_{s}.

2.3.8 Standard bias effects

In standard bias theory, the non-linear bias parameters connecting the galaxy density field and the dark matter density field appear in the growth and tidal terms of the density fluctuations. Thus, they are added to F_{g} and F_{t} as follows (for a review, see Desjacques et al. 2018):

$$\Delta F_{\mathrm{g}} = \frac{1}{2}\frac{b_2}{b_1}, \quad \Delta F_{\mathrm{t}} = \frac{b_{\mathrm{t}}}{b_1}, \tag{33}$$

where b_2 and b_{t} denote the local non-linear bias parameter and the tidal bias parameter, respectively. In this case, the condition $F_2(\boldsymbol{k}, -\boldsymbol{k}) = 0$, which is satisfied in the absence of the bias effect, does not hold, and F_{g} should be treated as an independent parameter, while G_{g} remains dependent.

2.3.9 Relative velocities

The relative velocity effects of baryons and cold dark matter, together with a corresponding bias parameter, enter the galaxy density fluctuation with a quadratic form (Dalal, Pen & Seljak 2010). The resulting shift term is modified in the second-order density fluctuation (Yoo et al. 2011),

$$\Delta F_{\mathrm{s}} = -\frac{b_r}{b_1}\frac{T_{\mathrm{rv}}(k_1)T_{\mathrm{rv}}(k_2)}{T_{\mathrm{m}}(k_1)T_{\mathrm{m}}(k_2)}, \tag{34}$$

where b_r denotes the relative velocity bias parameter, T_{rv} is the relative velocity transfer function, and T_{m} is the dark matter transfer function. This relative velocity effect on galaxy clustering has been measured using galaxy power spectra and 3PCFs, but its signature has not yet been detected (Yoo & Seljak 2013; Beutler et al. 2016; Slepian et al. 2018).

The relative velocity effect is obtained by the ratio of the relative velocity to the dark matter transfer functions $T_{\mathrm{rv}}(k)/T_{\mathrm{m}}(k)$, which is scale-dependent and therefore does not fit into the parameterization framework of this paper. However, if a signal with $E_{\mathrm{s}} \neq 1$ is detected, a correct physical interpretation would require a reanalysis to account for this possible relative velocity effect.

2.3.10 Extended bias effects

In this paper, we discuss the possibility of extended bias theories. For example, in specific gravity theories, such as DHOST theories, the coefficient of the density fluctuation shift term F_{s} deviates from 1, violating the LSS consistency relation. On the other hand, Fujita & Vlah (2020) showed that the standard bias theory is reproduced in theories that satisfy the LSS consistency relation. In other words, for DHOST theories with $F_{\mathrm{s}} \neq 1$, there may be an additional bias effect in F_{s}. Since the shift term is described by the product of the displacement vector and the density fluctuation, the bias of the shift term may be related to the bias effect of the displacement vector. Furthermore, since the time derivative of the displacement vector is a velocity field, the bias effect of the displacement vector may induce the bias effect of linear and non-linear velocity fields (see also section 9.12 in S23).

Based on the above considerations, we assume that bias effects occur for all non-linear parameters,

$$\Delta F_{\mathrm{g}} = \frac{1}{2}\frac{b_2}{b_1}, \quad \Delta F_{\mathrm{s}} = \frac{b_{\mathrm{s}}}{b_1}, \quad \Delta F_{\mathrm{t}} = \frac{b_{\mathrm{t}}}{b_1},$$
$$\Delta G_{\mathrm{g}} = \frac{1}{2} b_{v2}, \quad \Delta G_{\mathrm{s}} = b_{v\mathrm{s}}, \quad \Delta G_{\mathrm{t}} = b_{v\mathrm{t}}, \tag{35}$$

where b_{s} is the shift bias in the second-order density fluctuation, and b_{v2}, $b_{v\mathrm{s}}$, and $b_{v\mathrm{t}}$ are the non-linear local bias, shift bias, and tidal bias in the velocity fluctuation. In such an extended bias theory, the condition $G_2(\boldsymbol{k}, -\boldsymbol{k}) = 0$ no longer holds, and G_{g} should also be treated as an independent parameter. Since the assumption of a linear velocity bias does not change the form of equation (2), but only multiplies the velocity bias parameter b_v by f, we implicitly assume a linear velocity bias and use f as it is. Of course, numerical experiments such as N-body simulations of dark matter, including effects such as DHOST theories, are needed to verify this consideration. Such studies are left as future work.

2.4 Bispectrum and 3PCF models

The leading order galaxy power spectrum and bispectrum in perturbation theory are given by

$$\begin{aligned} P(\boldsymbol{k}) &= [Z_1(\boldsymbol{k})]^2 P_{\rm lin}(k), \\ B(\boldsymbol{k}_1, \boldsymbol{k}_2) &= 2 Z_2(\boldsymbol{k}_1, \boldsymbol{k}_2) Z_1(\boldsymbol{k}_1) Z_1(\boldsymbol{k}_2) P_{\rm lin}(k_1) P_{\rm lin}(k_2) \\ &\quad + (\boldsymbol{k}_1 \leftrightarrow \boldsymbol{k}_3) + (\boldsymbol{k}_2 \leftrightarrow \boldsymbol{k}_3), \end{aligned} \tag{36}$$

where $\boldsymbol{k}_1 + \boldsymbol{k}_2 + \boldsymbol{k}_3 = 0$.

The theoretical models in equation (36) work well in principle on large scales around and above $100\,h^{-1}$ Mpc, but they cannot describe the non-linear decay of the signal of the Baryon Acoustic Oscillations (BAOs; Peebles & Yu 1970; Sunyaev & Zeldovich 1970) that occurs around $100\,h^{-1}$ Mpc. In order to include the effects of the non-linear decay of the BAO, while preserving the form of the leading-order solutions of the power spectrum and the bispectrum, we use the following theoretical models, which are obtained by re-summing the IR modes appearing in the expansion via perturbation theory (Eisenstein, Seo & White 2007; Sugiyama et al. 2021),

$$\begin{aligned} P(\boldsymbol{k}) &= [Z_1(\boldsymbol{k})]^2 \left[\mathcal{D}^2(\boldsymbol{k}) P_{\rm w}(k) + P_{\rm nw}(k)\right], \\ B(\boldsymbol{k}_1, \boldsymbol{k}_2) &= 2\, Z_2(\boldsymbol{k}_1, \boldsymbol{k}_2) Z_1(\boldsymbol{k}_1) Z_1(\boldsymbol{k}_2) \\ &\quad \times \Big\{ \mathcal{D}(\boldsymbol{k}_1)\mathcal{D}(\boldsymbol{k}_2)\mathcal{D}(\boldsymbol{k}_3) P_{\rm w}(k_1) P_{\rm w}(k_2) \\ &\quad + \mathcal{D}^2(\boldsymbol{k}_1) P_{\rm w}(k_1) P_{\rm nw}(k_2) + \mathcal{D}^2(\boldsymbol{k}_2) P_{\rm nw}(k_1) P_{\rm w}(k_2) \\ &\quad + P_{\rm nw}(k_1) P_{\rm nw}(k_2) \Big\} + (\boldsymbol{k}_1 \leftrightarrow \boldsymbol{k}_3) + (\boldsymbol{k}_2 \leftrightarrow \boldsymbol{k}_3), \end{aligned} \tag{37}$$

where $P_{\rm lin}$ is decomposed into two parts: the ‘no-wiggle (nw)’ part $P_{\rm nw}$, which is a smooth version of $P_{\rm lin}$ with the baryon oscillations removed (Eisenstein & Hu 1998), and the ‘wiggle (w)’ part defined as $P_{\rm w} = P_{\rm lin} - P_{\rm nw}$. The non-linear BAO degradation is represented by the 2D Gaussian damping factor derived from a differential motion of Lagrangian displacements (Eisenstein et al. 2007; Crocce & Scoccimarro 2008; Matsubara 2008):

$$\mathcal{D}(\boldsymbol{k}) = \exp\left(-\frac{k^2(1-\mu^2)\sigma_\perp^2 + k^2\mu^2\sigma_\parallel^2}{2}\right), \tag{38}$$

where $\mu = \hat{k}\cdot\hat{n}$. We compute the radial and transverse components of the smoothing parameters, $\sigma_\perp$ and $\sigma_\parallel$, using the Zel’dovich approximation (Zel’Dovich 1970; Crocce & Scoccimarro 2008; Matsubara 2008):

$$\begin{aligned} \sigma_\perp^2 &= \frac{1}{3}\int \frac{dp}{2\pi^2} P_{\rm lin}(p), \\ \sigma_\parallel^2 &= (1+f)^2\, \sigma_\perp^2. \end{aligned} \tag{39}$$

We decompose the power spectrum into multipole components using Legendre polynomial functions $\mathcal{L}_\ell$ (e.g. Hamilton 1997),

$$P(\boldsymbol{k}) = \sum_\ell P_\ell(k) \mathcal{L}_\ell(\hat{k}\cdot\hat{n}). \tag{40}$$

The multipole components of the power spectrum are then related to those of the 2PCF by a 1D Hankel transformation,

$$\xi_\ell(r) = i^\ell \int \frac{dk k^2}{2\pi^2} j_\ell(rk) P_\ell(k), \tag{41}$$

where j_ℓ is the ℓ-th order spherical Bessel function. The multipole index ℓ refers to the expansion with respect to the line-of-sight dependence due to the Redshift Space Distortion effect (RSD; Kaiser 1987) and the Alcock–Paczyński effect (AP; Alcock & Paczyński 1979). The components with $\ell = 0$, 2, and 4 are called monopole, quadrupole, and hexadecapole, respectively; the components with $\ell > 0$ are caused only by the RSD effect and the AP effect.

We adopt the decomposition formalism of the bispectrum into multipole components using tri-polar spherical harmonic (TripoSH) base functions (Sugiyama et al. 2019),

$$B(\boldsymbol{k}_1, \boldsymbol{k}_2) = \sum_{\ell_1+\ell_2+\ell=\text{even}} B_{\ell_1\ell_2\ell}(k_1, k_2)\, \mathcal{S}_{\ell_1\ell_2\ell}(\hat{k}_1, \hat{k}_2, \hat{n}), \tag{42}$$

where the TripoSH base functions are given by

$$\begin{aligned} \mathcal{S}_{\ell_1\ell_2\ell}(\hat{k}_1, \hat{k}_2, \hat{n}) &= \frac{4\pi}{h_{\ell_1\ell_2\ell}} \sum_{m_1m_2m} \begin{pmatrix} \ell_1 & \ell_2 & \ell \\ m_1 & m_2 & m \end{pmatrix} \\ &\quad \times Y_{\ell_1m_1}(\hat{k}_1) Y_{\ell_2m_2}(\hat{k}_2) Y_{\ell m}(\hat{n}), \end{aligned}$$

with

$$h_{\ell_1\ell_2\ell} = \sqrt{\frac{(2\ell_1+1)(2\ell_2+1)(2\ell+1)}{4\pi}} \begin{pmatrix} \ell_1 & \ell_2 & \ell \\ 0 & 0 & 0 \end{pmatrix}. \tag{43}$$

The multipole components of the bispectrum are then related to those of the 3PCF by a 2D Hankel transformation,

$$\begin{aligned} \zeta_{\ell_1\ell_2\ell}(r_1, r_2) &= i^{\ell_1+\ell_2} \int \frac{dk_1 k_1^2}{2\pi^2} \int \frac{dk_2 k_2^2}{2\pi^2} \\ &\quad \times j_{\ell_1}(r_1k_1) j_{\ell_2}(r_2k_2) B_{\ell_1\ell_2\ell}(k_1, k_2). \end{aligned} \tag{44}$$

The multipole index ℓ appearing in $B_{\ell_1\ell_2\ell}$ or $\zeta_{\ell_1\ell_2\ell}$ is associated with the multipole expansion w.r.t. the line of sight, just as the index ℓ in the power spectrum, P_ℓ.

2.5 Theoretical predictions

Fig. 1 shows how the multipole components of the 3PCF are affected when the coefficients of the shift terms for density and velocity fluctuations, i.e. $F_{\rm s}$ and $G_{\rm s}$, are changed from 1. Since Section 4.2 will show that the 1σ error for $E_{\rm s}$ is about 3, we add ±3 to the $E_{\rm s} = 1$ value in ΛCDM to compute the cases where $E_{\rm s} = -2$ and $E_{\rm s} = 4$. In other words, we compute the four cases for ($F_{\rm s} = 0.25$, $G_{\rm s} = 1.0$), ($F_{\rm s} = -0.5$, $G_{\rm s} = 1.0$), ($F_{\rm s} = 1.0$, $G_{\rm s} = 4.0$), and ($F_{\rm s} = 1.0$, $G_{\rm s} = -2.0$).

Focusing on the monopole components, i.e. ζ_{000} and ζ_{110}, the effect of changing the value of $F_{\rm s}$ is more significant than when $G_{\rm s}$ is changed. This result suggests that the monopole component can constrain $F_{\rm s}$ well. Next, we look at the quadrupole components, i.e. ζ_{202} and ζ_{112}. Again, the change in $F_{\rm s}$ can affect them more than in $G_{\rm s}$, but the difference is less than for the monopole component. This fact means that $G_{\rm s}$ or $E_{\rm s}$ is determined in the quadrupole component after $F_{\rm s}$ has been determined in the monopole component.

Of course, in the actual MCMC analysis, not only $F_{\rm s}$ and $G_{\rm s}$ are varied, but also $F_{\rm g}$, $F_{\rm t}$, $G_{\rm g}$, and $G_{\rm t}$. The influence of all these parameters on the 3PCF multipole can be seen in figs 1–2 of S23.

3 DATA ANALYSIS METHODOLOGY

Our data analysis methods are summarized below. See S23 for details.

(i) To simplify the correction for window function effects, the 2PCF and the 3PCF are used instead of the power spectrum and the bispectrum in Fourier space, following Sugiyama et al. (2021, 2023).

(ii) Only large scales in the range $80\,h^{-1}\,{\rm Mpc} \le r \le 150\,h^{-1}\,{\rm Mpc}$ are used, where the 2PCF and 3PCF models (37) are expected to work well. This expectation has been confirmed in the context of GR by Sugiyama et al. (2021). Hirano et al. (2020) has shown that when the shift term deviates from 1, ultra-violet divergence appears in the non-linear correction term in the power spectrum, i.e. referred to as the one-loop term, leading to unattainable converged values.

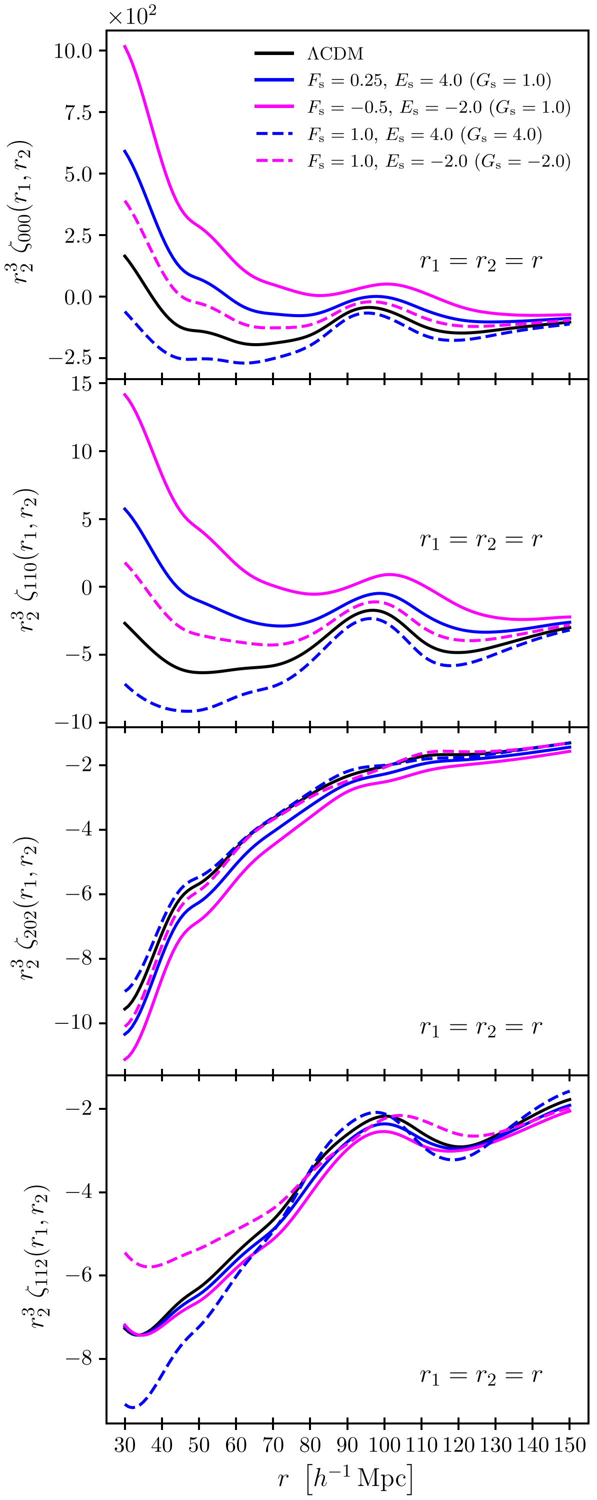

Figure 1. Multipole components of the 3PCF, i.e. ζ_{000}, ζ_{110}, ζ_{202}, and ζ_{112}, at $z = 0.61$, calculated from the theoretical model in equation (37), when the coefficients of the shift terms of the density or velocity fluctuations, i.e. F_s or G_s, vary from 1. The results are shown for $F_s = G_s = 1$ (black solid), $F_s = 0.25$ and $G_s = 1$ (blue solid), $F_s = -0.5$ and $G_s = 1$ (magenta solid), $F_s = 1$ and $G_s = 4.0$ (blue dashed), $F_s = 1$ and $G_s = -2.0$ (magenta dashed). For the sake of simplicity, the plot is made as a function of $r_1 = r_2 = r$. The cosmological parameters used to draw this plot are given in Section 1, and the assumed linear bias is $b_1 = 2$, and the assumed non-linear biases are zero, i.e. $b_2 = b_t = 0$.

Therefore, we expect similar behavior in the bispectrum and focus only on scales larger than $80\,h^{-1}$ Mpc, where the loop correction term will not make a significant contribution.

(iii) The bin widths are $5\,h^{-1}$ Mpc for the 2PCF and $10\,h^{-1}$ Mpc for the 3PCF; the 3PCF has a wider bin width than the 2PCF to reduce the number of data bins. These bin widths are the same as those used in Sugiyama et al. (2021) for the anisotropic BAO analysis using the 2PCF and 3PCF.

(iv) The multipole components of the 2PCF and 3PCF used in the analysis are ξ_0, ξ_2, ζ_{000}, ζ_{110}, ζ_{202}, and ζ_{112}. In particular, ζ_{000}, ζ_{110}, and ζ_{112} are only considered for $r_1 \geq r_2$ since $\zeta_{\ell_1\ell_2\ell}(r_1, r_2) = \zeta_{\ell_2\ell_1\ell}(r_2, r_1)$. In this case, the total number of data bins is 202.

(v) The multipole components of the 2PCF and 3PCF are measured using an FFT[2]-based estimator (Sugiyama et al. 2019). The theoretical models for the 2PCF and 3PCF are then computed according to section 4 in S23, taking into account the window function effect.

(vi) The eight parameters constrained in this analysis are $(b_1\sigma_8)$, $(f\sigma_8)$, $(F_g\sigma_8)$, $(F_s\sigma_8)$, $(F_t\sigma_8)$, $(G_g\sigma_8)$, E_s, and $(G_t\sigma_8)$; the constraint on the E_s parameter is the main result in this paper.

(vii) The AP effect (Alcock & Paczyński 1979) is ignored in our analysis. However, the AP effect can be determined by the 2PCF at a few per cent and is not expected to significantly affect the constraint results for the parameters that characterize the non-linear fluctuations of interest in this paper, such as E_s.

(viii) The galaxy data used in the analysis is the final galaxy clustering dataset, Data Release 12 (DR12; Alam et al. 2015) from the Baryon Oscillation Spectroscopic Survey (BOSS; Eisenstein et al. 2011; Bolton et al. 2012; Dawson et al. 2013). The BOSS survey includes four galaxy samples, CMASS, LOWZ, LOWZ2, and LOWZ3, which are combined into a single sample (Reid et al. 2016). This combined DR12 sample covers the redshift range $z =$ 0.2–0.75 and is divided into the two redshift bins, $0.2 < z < 0.5$ and $0.5 < z < 0.75$, which have the mean redshifts $z = 0.38$ and $z = 0.61$, respectively. Furthermore, the DR12 sample is observed across two galactic hemispheres, the Northern and Southern Galactic Caps, called NGC and SGC respectively. Thus, the four galaxy samples considered in our analysis are NGC at $z = 0.38$, SGC at $z = 0.38$, NGC at $z = 0.61$, and SGC at $z = 0.61$.

(ix) The 2PCF and 3PCF covariance matrices are computed by measuring the 2PCF and 3PCF from the publicly available 2048 MultiDark-Patchy mock catalogues (Patchy mocks; Kitaura et al. 2016; Klypin et al. 2016).

(x) For the NGC and SGC galaxy samples at $z = 0.38$, the p-values calculated from the best parameter values obtained by our analysis are less than 0.05, indicating that the theoretical 3PCF model does not fit the measurements well. The fact that such discrepancies between the data and the model occur even in a general parameter space suggests that this is likely to be an indication of systematics. Unfortunately, the reason for this cannot be identified in this paper. Therefore, following section 8 in S23, we multiplied the 3PCF covariance matrices measured from the NGC and SGC at $z = 0.38$ by a phenomenological pre-factor of 1.15 and 1.25, respectively, to increase the final p-value obtained. However, we found that this manipulation had little effect on the final E_s-constraint. This suggests that the degeneracy between the parameters is the main limitation of our analysis, rather than the 15–25 per cent changes in the 3PCF covariance matrices.

---

[2] Fast Fourier Transform

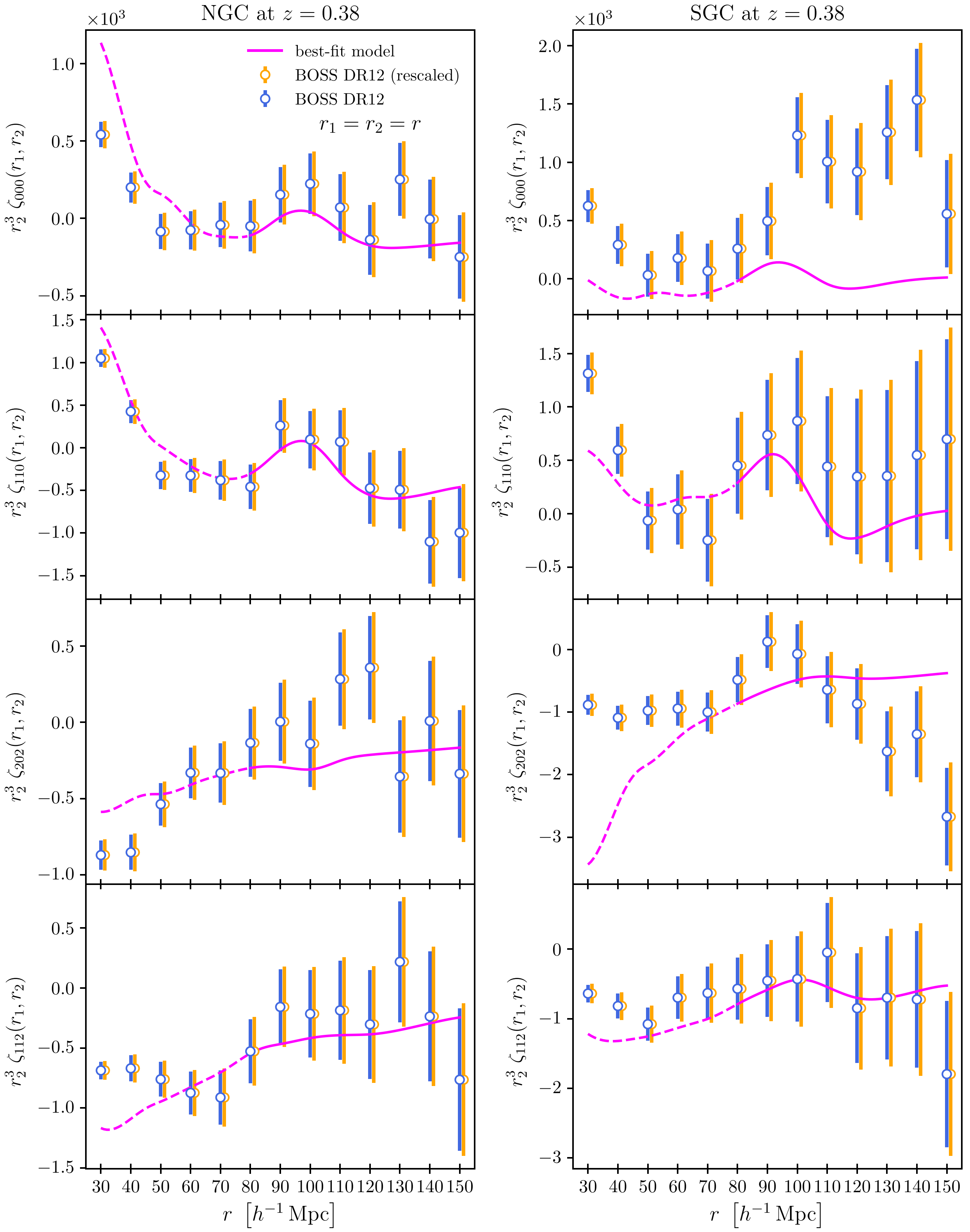

Figure 2. Multipole components of the 3PCF, i.e. ζ_{000}, ζ_{110}, ζ_{202}, and ζ_{112}, measured from the NGC and SGC samples at $z = 0.38$ (blue points). For the sake of simplicity, these plots are shown as a function of $r_1 = r_2 = r$, even though the actual MCMC analysis also uses the case $r_1 \neq r_2$. The error bars are the standard deviation of the 3PCF measurements computed from 2048 Patchy mocks. The orange error bars are the rescaled ones described in (x) of Section 3, which are used in the MCMC analysis. Also plotted are the theoretical models computed from the best-fitting parameter values obtained from the MCMC analysis (magenta lines); they are shown as solid lines at the scales $r \geq 80\,h^{-1}$ Mpc used in the analysis, and as dashed lines at smaller scales.

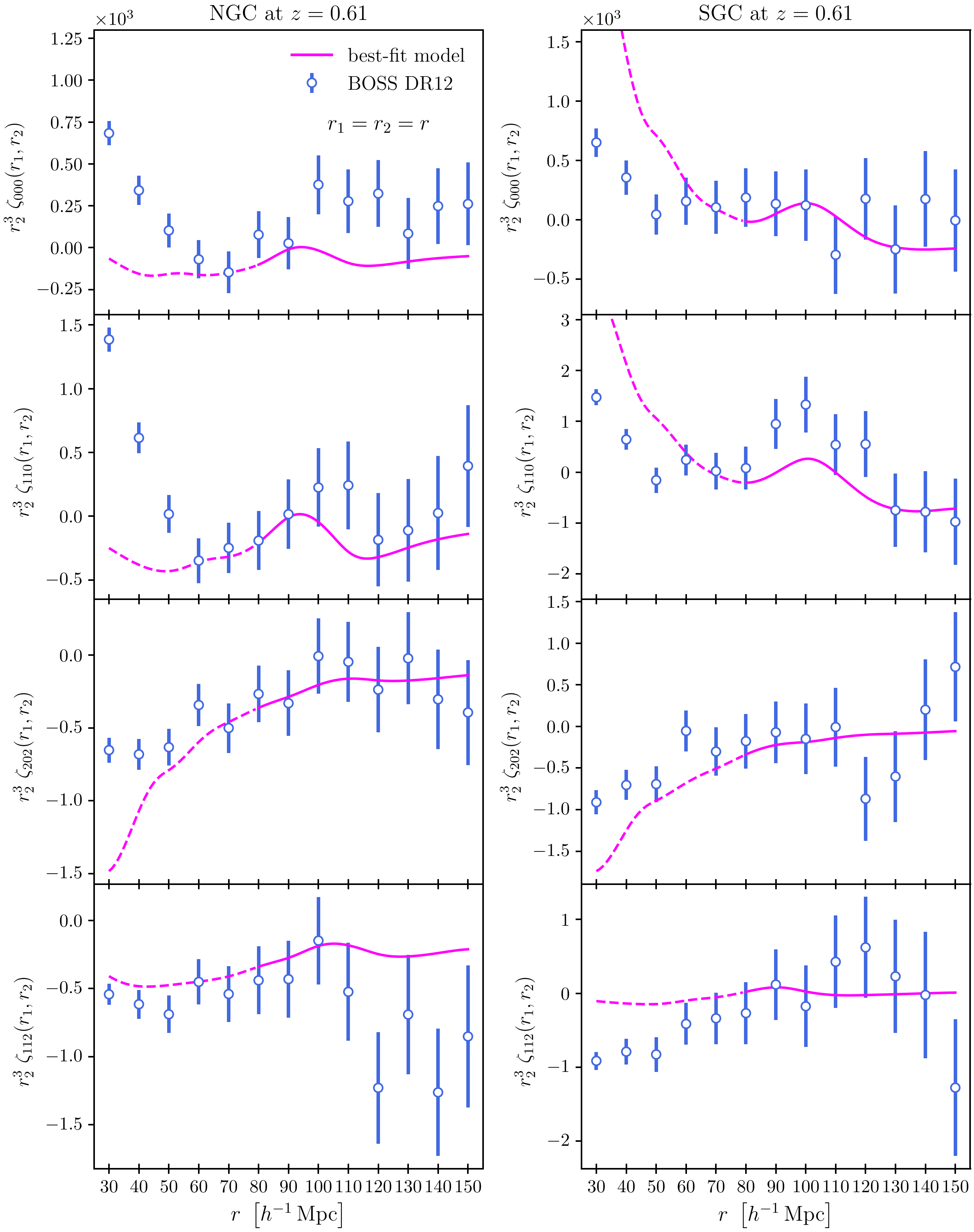

Figure 3. Same as Fig. 2, except that the results at $z = 0.61$ are shown.

(xi) The Hartlap [equation (17) in Hartlap, Simon & Schneider 2007] and M_1 [square root of equation (18) in Percival et al. 2014] factors are used to correct for the effect of errors in the covariance matrix, computed from a finite number of mock catalogues, on the final parameter errors. The M_2 factor [square root of equation (22) in Percival et al. 2014], obtained by combining the Hartlap and M_1 factors, is $M_2 = 1.105$ in our analysis, close enough to 1 for conservative data analysis.

(xii) The flat prior distribution of the parameter of interest is determined based on the error from a Fisher analysis, performed in the same setting as the main analysis. The fiducial parameter value $\theta_{\rm fid}$, assumed in performing the Fisher analysis, is calculated from the cosmological parameters introduced in Section 1 and the linear bias parameter $b_1 = 2$. With the standard deviation of the parameters obtained by the Fisher analysis being $\sigma_{\rm fisher}(\theta)$, then $\theta_{\rm fid} \pm 5\,\sigma_{\rm fid}(\theta)$ is used as the flat prior distribution.

(xiii) The likelihood of the parameters is computed using the MCMC algorithm implemented in MONTE PYTHON (Brinckmann & Lesgourgues 2019). We ensure the convergence of each MCMC chain by imposing $R - 1 \lesssim \mathcal{O}(10^{-4})$, where R is the standard Gelman–Rubin criteria (Gelman & Rubin 1992).

The convergence of the results is also checked through the following method. First, eight independent MCMC chains are generated, and the mean and standard deviation of the $E_{\rm s}$ parameter, $(E_{\rm s})_{\rm mean}$ and $(E_{\rm s})_{\rm std}$, are calculated from each chain. Next, the standard deviation of the mean, $((E_{\rm s})_{\rm mean})_{\rm std}$, and the mean of the standard deviation, $((E_{\rm s})_{\rm std})_{\rm mean}$, are calculated from the eight mean values and standard deviations. Finally, the ratio $((E_{\rm s})_{\rm mean})_{\rm std}/((E_{\rm s})_{\rm std})_{\rm mean}$ is checked to be less than 10 per cent. Our final $E_{\rm s}$ constraint is obtained by combining all eight chains into a single chain.

4 RESULTS

4.1 Measurements

Figs 2 and 3 show the multipole components of the 3PCF measured from the BOSS DR12 galaxies and the corresponding theoretical models calculated with the best-fitting parameters in Table A1. For the monopole components (ζ_{000} and ζ_{110}), a BAO peak is expected to appear around 100 h^{-1} Mpc. For example, ζ_{000} and ζ_{110} measured from NGC at $z = 0.38$ show a relatively clear BAO signal (see Fig. 2, upper left two panels), but the BAO signal is not seen in some galaxy samples. Also, as noted by S23 and discussed in (x) of Section 3, ζ_{000} measured from SGC at $z = 0.38$ shows statistically significant differences from the theoretical model on large scales (see Fig. 2, upper right-hand panel).

Although the 3PCF multipole, $\zeta_{\ell_1\ell_2\ell}$, is a function of r_1 and r_2, only the case $r_1 = r_2$ is plotted here to simplify the figure; see figs 12–19 in S23 for the results for $r_1 \neq r_2$.

4.2 Constraints on $E_{\rm s}$

Fig. 4 shows the 1D marginalized posterior probability distributions for $E_{\rm s}$, and Table 1 summarizes the results of constraining $E_{\rm s}$ computed from the posteriors. The results presented in this table show the results of constraining $E_{\rm s}$ separately for the four BOSS samples and a combination of these results.

The $E_{\rm s}$ constraint results from each sample of BOSS galaxies are helpful, for example, in constraining models that vary the coefficient of the shift term from 1, as presented in Sections 2.3.3, 2.3.7, 2.3.9, and 2.3.10.

On the other hand, from the point of view of examining the violation of the LSS consistency relation, it is also useful to combine all four galaxy samples to see if $E_{\rm s}$ is consistent with $E_{\rm s} = 1$. Such an analysis is possible because the predicted $E_{\rm s}$ value for any sample of galaxies and at any redshift is always $E_{\rm s} = 1$ if the LSS consistency relation is satisfied. The $E_{\rm s}$ value obtained in this analysis is no longer meaningful as a physical parameter, but is interpreted as a parameter for testing the LSS consistency relation. As a result, we obtain

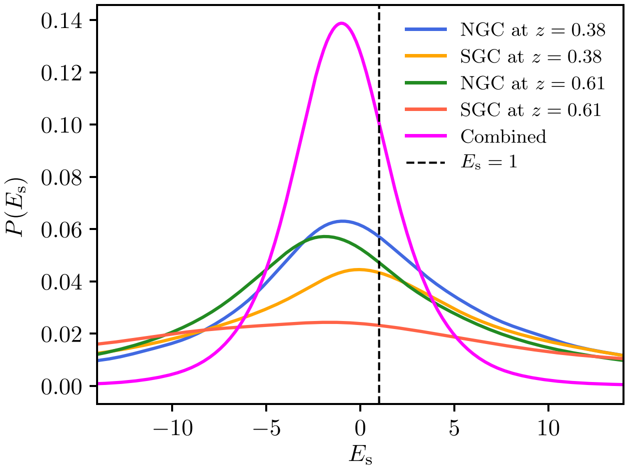

Figure 4. 1D marginalized posterior probability distributions for $E_{\rm s}$. Results are shown for NGC at $z = 0.38$ (blue), SGC at $z = 0.38$ (orange), NGC at $z = 0.61$ (green), SGC at $z = 0.61$ (red), and the four samples combined (magenta). A vertical line with $E_{\rm s} = 1$ (black dashed line) is also plotted, indicating that the consistency relation is satisfied.

$$E_{\rm s} = -0.92^{+3.13}_{-3.26} \tag{45}$$

at the 1σ level. This result indicates that the present analysis using the BOSS galaxy data does not violate the LSS consistency relation within the statistical error of the data.

4.3 Comparison with the results of the Fisher analysis

Table 1 shows that the errors obtained for each galaxy sample are larger than those predicted by the Fisher analysis, while the combined sample yields a constraint close to the Fisher estimate. This is because the tail of the posterior distribution function obtained for each galaxy sample is more widely spread out than the Gaussian function assumed in the Fisher analysis. On the other hand, when the four galaxy samples are combined, the posterior distribution function approaches the Gaussian function due to the central limit theorem; see Fig. 5 for a comparison of the posterior distribution function of $E_{\rm s}$ and the Gaussian distribution function.

4.4 Discussions for future research

In anticipation of future surveys, it is important to note that the magnitude of statistical errors is inversely proportional to the square root of the survey volume. Thus, it naturally follows that the larger the survey volume, the smaller the resulting errors. Currently, the volume of the BOSS data being used in this paper is roughly $4\,(h^{-1}\,{\rm Gpc})^3$. By comparison, the survey volume of the Dark Energy Spectroscopic Instrument (DESI; DESI Collaboration 2016)[3] is expected to reach $\sim 40\,(h^{-1}\,{\rm Gpc})^3$, which is ten times that of BOSS. Moreover, it is projected that by combining various galaxy surveys, such as Euclid (Laureijs et al. 2011)[4] and the Subaru Prime Focus Spectrograph (PFS; Takada et al. 2014),[5] we can anticipate an improvement in the current constraint results by a factor of 3-4.

---

[3] http://desi.lbl.gov/
[4] www.euclid-ec.org
[5] https://pfs.ipmu.jp/index.html

Table 1. Means, standard deviations, and $\pm 1\sigma$ errors (68.27 per cent CL) calculated from the $E_{\rm s}$ posteriors shown in Fig. 4.

	$(E_{\rm s})_{\rm mean}$	$(E_{\rm s})_{\rm std}$ (fisher)	$(E_{\rm s})_{-1\sigma}$	$(E_{\rm s})_{+1\sigma}$	$\chi^2_{\rm min}$/DoF (p-value)
NGC at $z = 0.38$	0.44	9.85 (5.40)	−8.93	8.32	207.2/194 (0.245)
SGC at $z = 0.38$	−1.69	16.08 (8.80)	−12.21	15.13	199.3/194 (0.382)
NGC at $z = 0.61$	−1.42	11.89 (6.95)	−9.77	9.93	216.6/194 (0.128)
SGC at $z = 0.61$	−7.32	23.93 (11.6)	−19.44	24.78	203.9/194 (0.299)
Combined four samples	−0.92	3.72 (3.64)	−3.26	3.13	-

Results are shown for each galaxy sample and for the four samples combined. The standard deviations of the parameters predicted by the Fisher analysis are given in round brackets. The rightmost column shows the reduced χ^2 computed from the best-fitting parameter values, and the corresponding p-values, where the degrees of freedom (DoF) are $202 - 8 = 194$.

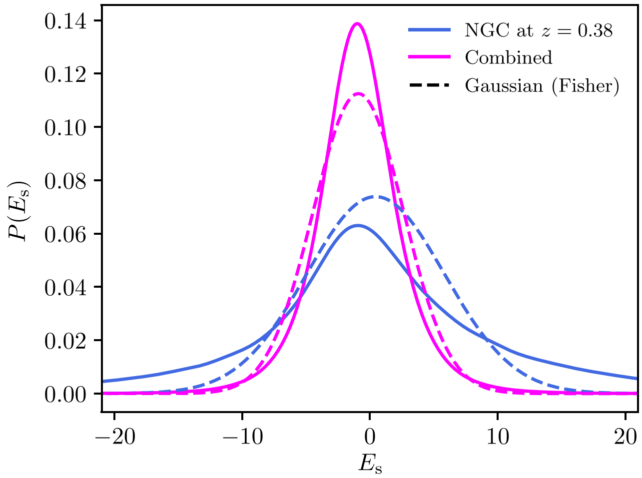

Figure 5. Same as Fig. 4, except that the Gaussian distribution functions assumed in the Fisher analysis are also plotted simultaneously as dashed lines. For clarity of display, only two cases are plotted, NGC at $z = 0.38$ and the combined sample. The Gaussian distributions are plotted with the mean value given in the $(E_{\rm s})_{\rm mean}$ column of Table 1 and the standard deviation predicted by the Fisher analysis input.

Furthermore, as demonstrated by Sugiyama et al. (2020), the shot noise effect determined by the galaxy number density is crucial in assessing statistical errors in the galaxy bispectrum and 3PCF. For example, in the BOSS case, it was shown in sections 5 and 7 of S23 that a smaller volume but high-density sample at $z = 0.38$ can impose stronger constraints on the non-linear parameters (3) using the 3PCF measurement compared to a larger volume but low-density sample at $z = 0.61$. Indeed, in this paper, the $E_{\rm s}$ results obtained in Table 1 show smaller errors for the $z = 0.38$ sample than for the $z = 0.61$ case. Although the galaxy number density for BOSS is $\sim 3 \times 10^{-4}\,(h^{-1}\,{\rm Mpc})^{-3}$, for DESI it can reach up to $\sim 7 \times 10^{-4}\,(h^{-1}\,{\rm Mpc})^{-3}$, depending on the redshift bin, enabling us to anticipate better constraints on $E_{\rm s}$, beyond the actual volume differences.

The prediction of the constraint results for the non-linear parameters using information on smaller scales than those used in this paper was carried out by the Fisher analysis in section 7 of S23 in the context of DHOST theories. In that case, for example, the coefficient $G_{\rm s}\sigma_8$ of the shift term in the non-linear velocity field is expected to have ∼6 times better error improvement when using up to $30\,h^{-1}$ Mpc, compared to our current analysis using scales greater than $80\,h^{-1}$ Mpc. This dramatic improvement in parameter constraints through the use of small scales serves as a strong motivation to further develop theoretical bispectrum models applicable to smaller scales.

The use of more multipole components than the four multipole components (ζ_{000}, ζ_{110}, ζ_{202}, and ζ_{112}) of the 3PCF used in this paper is also expected to improve the constraint results for $E_{\rm s}$ and the other non-linear parameters.

Finally, note that although all six non-linear parameters (3) are varied in this paper to consider as general a situation as possible, the number of free parameters to be varied is reduced in many cases when actually constraining the specific models presented in Section 2.3. For example, for the constraints on neutrino masses in Section 2.3.7, assuming the standard bias effects in Section 2.3.8, all the growth, shift, and tidal terms of the non-linear velocity field can be used to constrain the neutrino mass. The results will therefore be better than the constraint results in this paper, which use only $E_{\rm s}$.

5 CONCLUSIONS

This paper is the first work to test the consistency relation for the LSS from actual galaxy clustering data. We have made this analysis possible through a joint analysis of anisotropic 2PCFs and 3PCFs measured from the BOSS DR12 galaxy data. While the anisotropic component of the 3PCF (or bispectrum) has mainly been used to improve the results of the 2PCF-only analysis (e.g. Sugiyama et al. 2021; D'Amico et al. 2022b; Ivanov et al. 2023), the results of this paper open a new observational window for anisotropic 3PCF analysis.

The LSS consistency relation relates the three-point statistics in the squeezed limit to the two-point statistics. The squeezed limit corresponds to extracting only the shift terms that appear in the second-order density and velocity fluctuations, and the LSS consistency relation is satisfied when the coefficients of the shift terms, denoted $F_{\rm s}$ and $G_{\rm s}$ (3), are $F_{\rm s} = G_{\rm s} = 1$. Conversely, the LSS consistency relation breaks down when $F_{\rm s}$ and $G_{\rm s}$ deviate from 1, e.g. due to multicomponent fluids, modified gravity, and their associated bias effects. However, among the three symmetric wavenumbers, k_1, k_2, and k_3, on which the bispectrum depends, taking the squeezed limit $k_1 \to 0$, the dependence of the remaining k_2 and k_3 becomes exchange symmetric, cancelling the coefficient modifications of the shift terms and behaving as if the LSS consistency relation were satisfied (Crisostomi et al. 2020). Furthermore, we pointed out in Section 2.1 that the coefficients of the shift terms are degenerate with the parameter σ_8 and appear in the form of $(F_{\rm s}\sigma_8)$ and $(G_{\rm s}\sigma_8)$, so we cannot directly constrain $F_{\rm s}$ and $G_{\rm s}$.

Two crucial ideas for solving the problems in the above paragraph are presented in Sections 2.1 and 2.2. The first idea is to test the LSS consistency relation independently of σ_8 by defining the $E_{\rm s}$ parameter (5) as the ratio of $(G_{\rm s}\sigma_8)$ to $(F_{\rm s}\sigma_8)$ and checking whether

$E_{\rm s}$ deviates from 1. Note that $E_{\rm s} \neq 1$ is a sufficient but not a necessary condition for showing a violation of the LSS consistency relation, since there may be theories that satisfy $F_{\rm s} = G_{\rm s} \neq 1$. The second idea is to ensure that our results hold in as many different situations as possible, we constrain $E_{\rm s}$ in a general parameter space framework with the coefficients of the growth, tidal, and shift terms as free parameters. Section 2.3 provides examples of models that are and are not included in our proposed parameterization.

This analysis requires information about the non-linearity of the velocity field, which requires dealing with the anisotropic component of the galaxy three-point statistic caused by the RSD effect. In this paper, we adopt a method of decomposing the anisotropic 3PCF using the TripoSH basis function in Section 2.4. This analysis method has been established in a series of papers by Sugiyama et al. (2019, 2021, 2023). In particular, our analysis method is similar to the one used in Sugiyama et al. (2023) to test DHOST theories from BOSS galaxies, except for the different parameters treated. Therefore, those interested in learning more about the analysis methods discussed in Section 3 are referred to that paper.

We have constrained $E_{\rm s}$ from two perspectives using the four galaxy samples from BOSS DR12. The first is a constraint on $E_{\rm s}$ from each galaxy sample that allows a physical interpretation by a specific model, as presented in Section 2.3. The second focuses on the violation of the LSS consistency relation and examines whether $E_{\rm s}$ deviates from 1 using the combined four samples. In this case, $E_{\rm s}$ is no longer interpreted as a physical parameter but as a parameter for testing the LSS consistency relation. In both cases, the results are consistent with $E_{\rm s} = 1$ within the 1σ error, as shown in Table 1. In particular, in the second case we obtained $E_{\rm s} = -0.92^{+3.13}_{-3.26}$. The results of this paper indicate that the LSS consistency relation is not violated within the statistical errors of the data in this analysis using the BOSS galaxy data.

In the future, several extensions can be made. First, it should be possible to include more 3PCF multipole components in the analysis. Secondly, the AP effect should be included in the analysis, and degeneracy relations between parameters with the AP effect should be considered. Finally, an attempt should be also made to improve the theoretical model of the 3PCF to include information at smaller scales. While attempting these improvements, the present analysis can be directly applied to upcoming spectroscopic galaxy surveys, such as DESI, Euclid, and PFS.

ACKNOWLEDGEMENTS

NSS acknowledges financial support from JSPS KAKENHI Grant Number 19K14703. Numerical computations were carried out on Cray XC50 at Center for Computational Astrophysics, National Astronomical Observatory of Japan. The work of TK was supported by JSPS KAKENHI Grant No. JP20K03936 and MEXT-JSPS Grant-in-Aid for Transformative Research Areas (A) 'Extreme Universe', No. JP21H05182 and No. JP21H05189. The work of DY was supported in part by JSPS KAKENHI Grants No. 19H01891, No. 22K03627. SS acknowledges the support for this work from NSF-2219212. SS is supported in part by World Premier International Research Center Initiative (WPI Initiative), MEXT, Japan. H-JS is supported by the U.S. Department of Energy, Office of Science, Office of High Energy Physics under DE-SC0019091 and DE-SC0023241. This project has received funding from the European Research Council (ERC) under the European Union's Horizon 2020 research and innovation program (grant agreement 853291). FB is a University Research Fellow.

DATA AVAILABILITY

The data underlying this article are available at the SDSS database (https://www.sdss.org/dr12/). A complete set of codes for data analysis is packaged under the name HITOMI and is publicly available at https://www.github.com/naonori/hitomi.git.

REFERENCES

Aghanim N., et al., 2020, A&A, 641, A6
Alam S., et al., 2015, ApJS, 219, 12
Alam S., et al., 2017, MNRAS, 470, 2617
Alcock C., Paczyński B., 1979, Nature, 281, 358
Bartolo N., Bellini E., Bertacca D., Matarrese S., 2013, J. Cosmol. Astropart. Phys., 2013, 34
Bellini E., Jimenez R., Verde L., 2015, J. Cosmol. Astropart. Phys., 2015, 57
Bernardeau F., Brax P., 2011, J. Cosmol. Astropart. Phys., 2011, 19
Berezhiani L., Khoury J., 2014, J. Cosmol. Astropart. Phys., 2014, 18
Bernardeau F., Colombi S., Gaztanaga E., Scoccimarro R., 2002, Phys. Rept., 367, 1
Bernardeau F., Van de Rijt N., Vernizzi F., 2012, Phys. Rev. D, 85, 63509
Bernardeau F., Van de Rijt N., Vernizzi F., 2013, Phys. Rev. D, 87, 43530
Beutler F., Blake C., Koda J., Marin F., Seo H.-J., Cuesta A. J., Schneider D. P., 2016, MNRAS, 455, 3230
Blas D., Lesgourgues J., Tram T., 2011, J. Cosmol. Astropart. Phys., 2011, 34
Blas D., Garny M., Konstandin T., 2013, J. Cosmol. Astropart. PHYS., 2013, 24
Blas D., Garny M., Ivanov M. M., Sibiryakov S., 2016, J. Cosmol. Astropart. Phys., 2016, 52
Bolton A. S., et al., 2012, AJ, 144, 144
Bose B., Koyama K., 2016, J. Cosmol. Astropart. Phys., 2016, 32
Bouchet F. R., Juszkiewicz R., Colombi S., Pellat R., 1992, ApJ, 394, L5
Bouchet F. R., Colombi S., Hivon E., Juszkiewicz R., 1995, A&A, 296, 575
Brinckmann T., Lesgourgues J., 2019, Phys. Dark Universe, 24, 100260
Burrage C., Dombrowski J., Saadeh D., 2019, J. Cosmol. Astropart. Phys., 2019, 23
Cabass G., Ivanov M. M., Philcox O. H. E., Simonović M., Zaldarriaga M., 2022a, Phys. Rev. D, 106, 43506
Cabass G., Ivanov M. M., Philcox O. H. E., Simonović M., Zaldarriaga M., 2022b, Phys. Rev. Lett., 129, 21301
Capozziello S., Francaviglia M., 2008, Gen. Rel. Grav., 40, 357
Creminelli P., Zaldarriaga M., 2004, J. Cosmol. Astropart. Phys., 2004, 6
Creminelli P., Noreña J., Simonović M., Vernizzi F., 2013, J. Cosmol. Astropart. Phys., 2013, 25
Creminelli P., Gleyzes J., Simonović M., Vernizzi F., 2014a, J. Cosmol. Astropart. Phys., 2014, 51
Creminelli P., Gleyzes J., Hui L., Simonović M., Vernizzi F., 2014b, J. Cosmol. Astropart. Phys., 2014, 9
Crisostomi M., Lewandowski M., Vernizzi F., 2020, Phys. Rev. D, 101, 123501
Crocce M., Scoccimarro R., 2008, Phys. Rev. D, 77, 23533
d'Amico G., Gleyzes J., Kokron N., Markovic K., Senatore L., Zhang P., Beutler F., Gil-Marín H., 2020, J. Cosmol. Astropart. Phys., 2020, 5
D'Amico G., Lewandowski M., Senatore L., Zhang P., 2022a, preprint (arXiv:2201.11518)
D'Amico G., Donath Y., Lewandowski M., Senatore L., Zhang P., 2022b, preprint (arXiv:2206.08327)
DESI Collaboration, 2016, preprint (arXiv:1611.00036)
Dalal N., Pen U.-L., Seljak U., 2010, J. Cosmol. Astropart. Phys., 2010, 7
Dawson K. S., et al., 2013, AJ, 145, 10
Deffayet C., Gao X., Steer D. A., Zahariade G., 2011, Phys. Rev. D, 84, 64039
Desjacques V., Jeong D., Schmidt F., 2018, Phys. Rept., 733, 1
Di Valentino E., Gariazzo S., Mena O., 2021, Phys. Rev. D, 104, 83504
Dvali G. R., Gabadadze G., Porrati M., 2000, Phys. Lett. B, 485, 208
Eisenstein D. J., Hu W., 1998, ApJ, 496, 605
Eisenstein D. J., Seo H.-j., White M. J., 2007, ApJ, 664, 660

Eisenstein D. J., et al., 2011, AJ, 142, 72
Esposito A., Hui L., Scoccimarro R., 2019, Phys. Rev. D, 100, 43536
Fasiello M., Fujita T., Vlah Z., 2022, Phys. Rev. D, 106, 123504
Frigo M., Johnson S. G., 2005, Proc. IEEE, 93, 216
Fujita T., Vlah Z., 2020, J. Cosmol. Astropart. Phys., 2020, 59
Gelman A., Rubin D. B., 1992, Stat. Sci., 7, 457
Gil-Marín H., Percival W. J., Verde L., Brownstein J. R., Chuang C.-H., Kitaura F.-S., Rodríguez-Torres S. A., Olmstead M. D., 2017, MNRAS, 465, 1757
Goldstein S., Esposito A., Philcox O. H. E., Hui L., Hill J. C., Scoccimarro R., Abitbol M. H., 2022, Phys. Rev. D, 106, 123525
Hahn T., 2005, Comput. Phys. Commun., 168, 78
Hamilton A. J. S., 1997, in Ringberg Workshop on Large Scale Structure Ringberg, Germany, September 23-28, 1996, preprint(arXiv:astro-ph/9708102)
Hamilton A. J. S., 2000, MNRAS, 312, 257
Hartlap J., Simon P., Schneider P., 2007, A&A, 464, 399
Hirano S., Kobayashi T., Tashiro H., Yokoyama S., 2018, Phys. Rev. D, 97, 103517
Hirano S., Kobayashi T., Yamauchi D., Yokoyama S., 2020, Phys. Rev. D, 102, 103505
Horndeski G. W., 1974, Int. J. Theor. Phys., 10, 363
Hu W., Sawicki I., 2007, Phys. Rev. D, 76, 64004
Inomata K., Lee H., Hu W., 2023, preprint (arXiv:2304.10559)
Ivanov M. M., Philcox O. H. E., Cabass G., Nishimichi T., Simonović M., Zaldarriaga M., 2023, Phys. Rev. D, 107, 83515
Jain B., Bertschinger E., 1996, ApJ, 456, 43
Kaiser N., 1987, MNRAS, 227, 1
Kamalinejad F., Slepian Z., 2020, preprint (arXiv:2011.00899)
Kehagias A., Riotto A., 2013, Nucl. Phys. B, 873, 514
Kitaura F.-S., et al., 2016, MNRAS, 456, 4156
Klypin A., Yepes G., Gottlober S., Prada F., Hess S., 2016, MNRAS, 457, 4340
Kobayashi T., 2019, Rept. Prog. Phys., 82, 86901
Kobayashi T., Yamaguchi M., Yokoyama J., 2011, Prog. Theor. Phys., 126, 511
Koyama K., Taruya A., Hiramatsu T., 2009, Phys. Rev. D, 79, 123512
Langlois D., 2019, Int. J. Mod. Phys. D, 28, 1942006
Laureijs R. et al., 2011, preprint (arXiv:1110.3193)
Lewandowski M., 2020, J. Cosmol. Astropart. Phys., 2020, 44
Lewandowski M., Senatore L., 2017, J. Cosmol. Astropart. Phys., 2017, 37
Lewandowski M., Perko A., Senatore L., 2015, J. Cosmol. Astropart. Phys., 2015, 19
Maldacena J. M., 2003, J. High Energy Phys., 2003, 13
Matsubara T., 2008, Phys. Rev., D77, 63530
Pearson D. W., Samushia L., 2018, MNRAS, 478, 4500
Peebles P. J. E., Yu J. T., 1970, ApJ, 162, 815
Peloso M., Pietroni M., 2013, J. Cosmol. Astropart. Phys., 2013, 31
Peloso M., Pietroni M., 2014, J. Cosmol. Astropart. Phys., 2014, 11
Percival W. J., et al., 2014, MNRAS, 439, 2531
Philcox O. H. E., Ivanov M. M., 2022, Phys. Rev. D, 105, 43517
Reid B., et al., 2016, MNRAS, 455, 1553
Schmittfull M., Baldauf T., Seljak U., 2015, Phys. Rev. D, 91, 43530
Scoccimarro R., Frieman J., 1996, ApJS, 105, 37
Scoccimarro R., Couchman H. M. P., Frieman J. A., 1999, ApJ, 517, 531
Slepian Z., Eisenstein D. J., 2017, MNRAS, 469, 2059
Slepian Z., et al., 2017, MNRAS, 469, 1738
Slepian Z., et al., 2018, MNRAS, 474, 2109
Sotiriou T. P., 2006, Class. Quantum Gravity, 23, 5117
Sotiriou T. P., Faraoni V., 2010, Rev. Mod. Phys., 82, 451
Sugiyama N. S., Futamase T., 2013, ApJ, 769, 106
Sugiyama N. S., Spergel D. N., 2014, J. Cosmol. Astropart. Phys., 2014, 42
Sugiyama N. S., Saito S., Beutler F., Seo H.-J., 2019, MNRAS, 484, 364
Sugiyama N. S., Saito S., Beutler F., Seo H.-J., 2020, MNRAS, 497, 1684
Sugiyama N. S., Saito S., Beutler F., Seo H.-J., 2021, MNRAS, 501, 2862
Sugiyama N. S. et al., 2023, MNRAS, 523, 3133
Sunyaev R. A., Zeldovich Y. B., 1970, Astrophys. Space Sci., 7, 3
Takada M., Komatsu E., Futamase T., 2006, Phys. Rev. D, 73, 83520
Takada M., et al., 2014, Publ. Astron. Soc. Jap., 66, R1
Takushima Y., Terukina A., Yamamoto K., 2014, Phys. Rev. D, 89, 104007
Tram T., Fidler C., Crittenden R., Koyama K., Pettinari G. W., Wands D., 2016, J. Cosmol. Astropart. Phys., 2016, 58
Tseliakhovich D., Hirata C., 2010, Phys. Rev. D, 82, 83520
Valageas P., Taruya A., Nishimichi T., 2017, Phys. Rev. D, 95, 23504
Yamauchi D., Sugiyama N. S., 2022, Phys. Rev. D, 105, 63515
Yamauchi D., Yokoyama S., Tashiro H., 2017, Phys. Rev. D, 96, 123516
Yoo J., Seljak U., 2013, Phys. Rev. D, 88, 103520
Yoo J., Dalal N., Seljak U., 2011, J. Cosmol. Astropart. Phys., 2011, 18
Zel'Dovich Y. B., 1970, A&A, 500, 13

APPENDIX A: OTHER NON-LINEAR PARAMETERS

While the main text focuses only on the results for $E_{\rm s}$, this appendix summarizes the results for the other parameters [see (vi) in Section 3] that were varied simultaneously in the MCMC analysis. Results for $G_{\rm s}\sigma_8$ are also reported as $G_{\rm s}\sigma_8 = (F_{\rm s}\sigma_8)\,E_{\rm s}$. Table A1 shows the best-fitting values, means, and standard deviations obtained from the four BOSS samples for the two parameters appearing in linear theory ($b_1\sigma_8$ and $f\sigma_8$) and for the six non-linear parameters ($F_{\rm g}\sigma_8$, $F_{\rm s}\sigma_8$, $F_{\rm t}\sigma_8$, $G_{\rm g}\sigma_8$, $G_{\rm s}\sigma_8$, $G_{\rm t}\sigma_8$). The covariance matrices for these parameters are shown in Table A2. For illustration, the marginalized 1D and 2D posteriors of the parameters are plotted for NGC at $z = 0.38$. The results presented in Tables A1 and A2 should not only be used to test the LSS consistency relation, which is the subject of this paper but can also be used directly to constrain the various specific models presented in Section 2.3.

In addition to the $E_{\rm s} \neq 1$ condition, it can also be argued that a signal $F_{\rm s}\sigma_8 < 0$ is a violation of the LSS consistency relation if it is found (see Section 2.2). Therefore, the results on $F_{\rm s}\sigma_8$ from Table A1 are summarized as follows:

$$F_{\rm s}\sigma_8 = \begin{cases} 0.715 \pm 0.685 & (\text{NGC at } z = 0.38) \\ 0.656 \pm 1.62 & (\text{SGC at } z = 0.38) \\ 0.883 \pm 0.845 & (\text{NGC at } z = 0.61) \\ 0.612 \pm 1.18 & (\text{SGC at } z = 0.61) \end{cases}. \tag{A1}$$

As shown above, since $F_{\rm s}\sigma_8 < 0$ cannot be statistically significant, it can be concluded that no violation of the LSS consistency relation was found in the current analysis.

Table A1. Best-fitting values, means, and standard deviations for $(b_1\sigma_8)$, $(f\sigma_8)$, $(F_{\rm g}\sigma_8)$, $(F_{\rm s}\sigma_8)$, $(F_{\rm t}\sigma_8)$, $(G_{\rm g}\sigma_8)$, $(G_{\rm s}\sigma_8)$, and $(G_{\rm t}\sigma_8)$ obtained in the joint analysis of the 2PCF and the 3PCF using the four BOSS samples.

NGC at $z = 0.38$								
	$b_1\sigma_8$	$f\sigma_8$	$F_{\rm g}\sigma_8$	$F_{\rm s}\sigma_8$	$F_{\rm t}\sigma_8$	$G_{\rm g}\sigma_8$	$G_{\rm s}\sigma_8$	$G_{\rm t}\sigma_8$
Best-fitting	1.35	0.469	1.20	0.753	−0.109	−1.80	−0.0987	2.00
Mean	1.23	0.433	1.32	0.715	−0.0191	−2.47	0.53	2.75
Std.	0.18	0.107	0.715	0.685	0.452	2.54	4.43	2.08
SGC at $z = 0.38$								
	$b_1\sigma_8$	$f\sigma_8$	$F_{\rm g}\sigma_8$	$F_{\rm s}\sigma_8$	$F_{\rm t}\sigma_8$	$G_{\rm g}\sigma_8$	$G_{\rm s}\sigma_8$	$G_{\rm t}\sigma_8$
Best-fitting	1.19	0.569	0.142	1.65	−1.25	5.58	2.12	−0.613
Mean	0.627	0.681	0.907	0.656	−0.47	4.35	4.93	−1.36
Std.	0.316	0.263	2.38	1.62	1.37	4.71	12.7	5.34
NGC at $z = 0.61$								
	$b_1\sigma_8$	$f\sigma_8$	$F_{\rm g}\sigma_8$	$F_{\rm s}\sigma_8$	$F_{\rm t}\sigma_8$	$G_{\rm g}\sigma_8$	$G_{\rm s}\sigma_8$	$G_{\rm t}\sigma_8$
Best-fitting	1.27	0.366	0.107	0.911	−0.191	3.24	−0.882	0.00682
Mean	1.08	0.361	−0.0782	0.883	0.0875	2.91	−0.633	0.393
Std.	0.158	0.109	0.868	0.845	0.574	3.05	7.85	2.7
SGC at $z = 0.61$								
	$b_1\sigma_8$	$f\sigma_8$	$F_{\rm g}\sigma_8$	$F_{\rm s}\sigma_8$	$F_{\rm t}\sigma_8$	$G_{\rm g}\sigma_8$	$G_{\rm s}\sigma_8$	$G_{\rm t}\sigma_8$
Best-fitting	1.27	0.266	1.45	−0.294	1.37	5.34	5.96	−9.76
Mean	0.943	0.312	1.41	0.612	1.73	3.8	0.0212	−6.57
Std.	0.235	0.168	1.93	1.18	1.12	6.81	25.3	4.24

The results for $(G_{\rm s}\sigma_8) = (F_{\rm s}\sigma_8)E_{\rm s}$ have been obtained from the MCMC chain of $E_{\rm s}$ and $(F_{\rm s}\sigma_8)$.

Table A2. Covariance matrices for $(b_1\sigma_8)$, $(f\sigma_8)$, $(F_{\rm g}\sigma_8)$, $(F_{\rm s}\sigma_8)$, $(F_{\rm t}\sigma_8)$, $(G_{\rm g}\sigma_8)$, $(G_{\rm s}\sigma_8)$, and $(G_{\rm t}\sigma_8)$ obtained in the joint analysis of the 2PCF and the 3PCF using the four BOSS samples.

NGC at $z = 0.38$								
	$b_1\sigma_8$	$f\sigma_8$	$F_{\rm g}\sigma_8$	$F_{\rm s}\sigma_8$	$F_{\rm t}\sigma_8$	$G_{\rm g}\sigma_8$	$G_{\rm s}\sigma_8$	$G_{\rm t}\sigma_8$
$b_1\sigma_8$	0.0318	−0.0109	−0.0192	−0.028	0.00321	−0.0864	−0.161	−0.0477
$f\sigma_8$	−0.0109	0.0112	0.00192	0.00325	−0.000899	0.0823	−0.0241	−0.0288
$F_{\rm g}\sigma_8$	−0.0192	0.00192	0.521	0.0496	0.151	−0.968	−0.425	−0.103
$F_{\rm s}\sigma_8$	−0.028	0.00325	0.0496	0.593	−0.236	0.155	−1.02	0.404
$F_{\rm t}\sigma_8$	0.00321	−0.000899	0.151	−0.236	0.22	−0.313	0.0416	−0.327
$G_{\rm g}\sigma_8$	−0.0864	0.0823	−0.968	0.155	−0.313	6.26	3.64	−1.58
$G_{\rm s}\sigma_8$	−0.161	−0.0241	−0.425	−1.02	0.0416	3.64	20.4	−4.52
$G_{\rm t}\sigma_8$	−0.0477	−0.0288	−0.103	0.404	−0.327	−1.58	−4.52	4.09
SGC at $z = 0.38$								
	$b_1\sigma_8$	$f\sigma_8$	$F_{\rm g}\sigma_8$	$F_{\rm s}\sigma_8$	$F_{\rm t}\sigma_8$	$G_{\rm g}\sigma_8$	$G_{\rm s}\sigma_8$	$G_{\rm t}\sigma_8$
$b_1\sigma_8$	0.0865	−0.0422	0.0464	0.0969	−0.0934	−0.0671	−0.279	0.0788
$f\sigma_8$	−0.0422	0.0631	−0.0558	−0.0621	0.0296	0.00688	−0.404	−0.202
$F_{\rm g}\sigma_8$	0.0464	−0.0558	4.51	0.296	0.435	−3.5	−0.245	0.0227
$F_{\rm s}\sigma_8$	0.0969	−0.0621	0.296	3.31	−0.516	0.433	−3.37	−0.0595
$F_{\rm t}\sigma_8$	−0.0934	0.0296	0.435	−0.516	1.99	−0.549	−0.63	−1.27
$G_{\rm g}\sigma_8$	−0.0671	0.00688	−3.5	0.433	−0.549	22.5	12.6	−11.5
$G_{\rm s}\sigma_8$	−0.279	−0.404	−0.245	−3.37	−0.63	12.6	171	−17.9
$G_{\rm t}\sigma_8$	0.0788	−0.202	0.0227	−0.0595	−1.27	−11.5	−17.9	27.6
NGC at $z = 0.61$								
	$b_1\sigma_8$	$f\sigma_8$	$F_{\rm g}\sigma_8$	$F_{\rm s}\sigma_8$	$F_{\rm t}\sigma_8$	$G_{\rm g}\sigma_8$	$G_{\rm s}\sigma_8$	$G_{\rm t}\sigma_8$
$b_1\sigma_8$	0.024	−0.00748	0.0309	−0.0267	−0.018	−0.0598	−0.0707	−0.0294
$f\sigma_8$	−0.00748	0.0117	−0.0141	−0.00346	0.00278	0.0298	0.0602	0.00315
$F_{\rm g}\sigma_8$	0.0309	−0.0141	0.806	0.0312	0.204	−1.49	−0.814	−0.332
$F_{\rm s}\sigma_8$	−0.0267	−0.00346	0.0312	0.894	−0.311	0.00472	−2.62	0.776
$F_{\rm t}\sigma_8$	−0.018	0.00278	0.204	−0.311	0.37	−0.317	0.347	−0.705
$G_{\rm g}\sigma_8$	−0.0598	0.0298	−1.49	0.00472	−0.317	9.46	6.37	−2.09
$G_{\rm s}\sigma_8$	−0.0707	0.0602	−0.814	−2.62	0.347	6.37	43.3	−10.1
$G_{\rm t}\sigma_8$	−0.0294	0.00315	−0.332	0.776	−0.705	−2.09	−10.1	7.75
SGC at $z = 0.61$								
	$b_1\sigma_8$	$f\sigma_8$	$F_{\rm g}\sigma_8$	$F_{\rm s}\sigma_8$	$F_{\rm t}\sigma_8$	$G_{\rm g}\sigma_8$	$G_{\rm s}\sigma_8$	$G_{\rm t}\sigma_8$
$b_1\sigma_8$	0.0576	−0.0196	0.0903	−0.0844	−0.0668	−0.116	−0.625	−0.171
$f\sigma_8$	−0.0196	0.0298	−0.0581	−0.0324	0.0214	0.135	1.19	−0.0697
$F_{\rm g}\sigma_8$	0.0903	−0.0581	3.99	0.155	0.508	−5.36	−4.29	−0.585
$F_{\rm s}\sigma_8$	−0.0844	−0.0324	0.155	2.6	−0.453	−0.126	−13.3	1.39
$F_{\rm t}\sigma_8$	−0.0668	0.0214	0.508	−0.453	1.14	−0.607	−0.467	−1.1
$G_{\rm g}\sigma_8$	−0.116	0.135	−5.36	−0.126	−0.607	44.9	24.5	−6.81
$G_{\rm s}\sigma_8$	−0.625	1.19	−4.29	−13.3	−0.467	24.5	651	−33.1
$G_{\rm t}\sigma_8$	−0.171	−0.0697	−0.585	1.39	−1.1	−6.81	−33.1	26.6

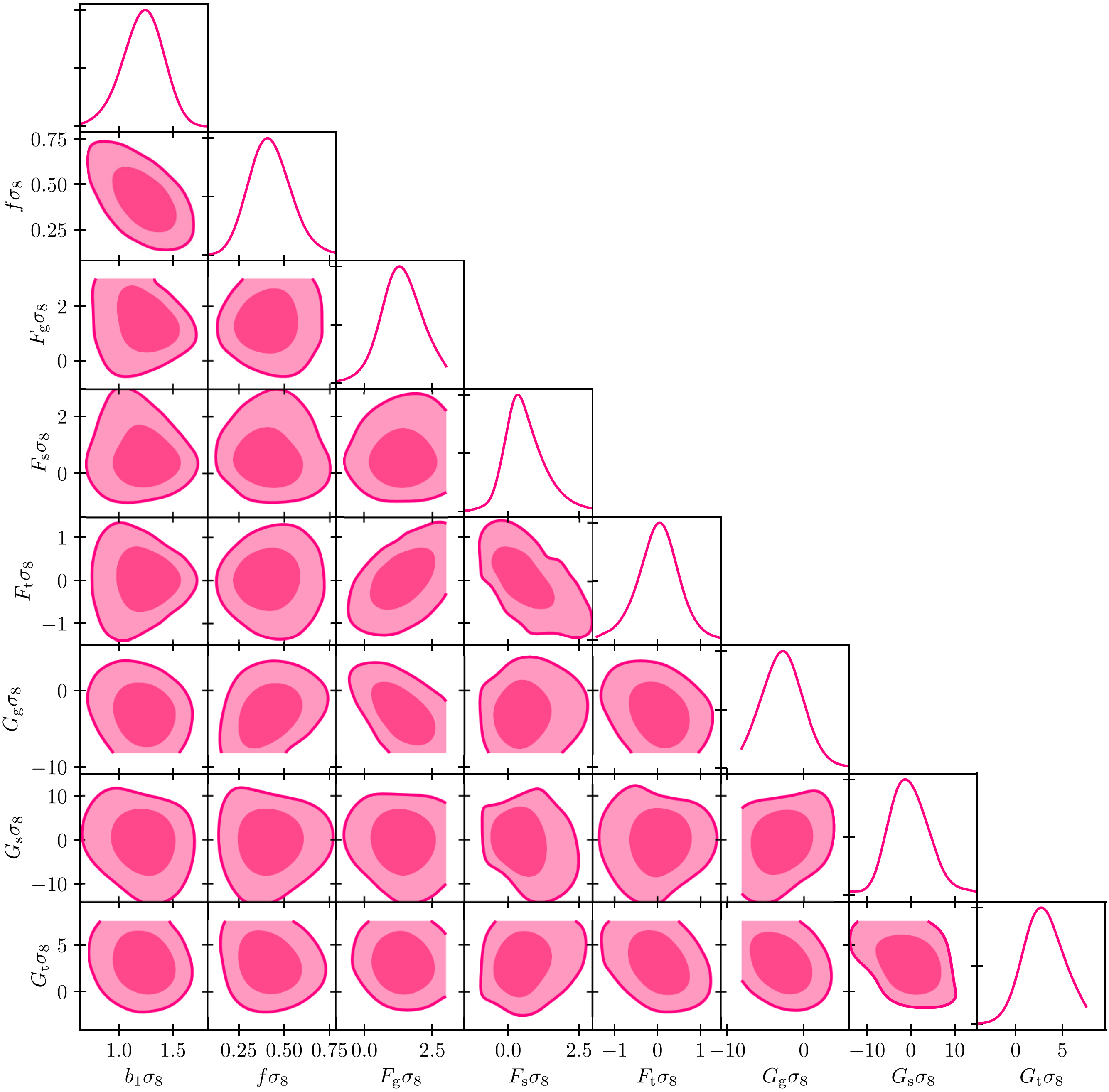

Figure A1. Marginalized 2D and 1D posteriors of the parameters ($b_1\sigma_8$), ($f\sigma_8$), ($F_g\sigma_8$), ($F_s\sigma_8$), ($F_t\sigma_8$), ($G_g\sigma_8$), ($G_s\sigma_8$), and ($G_t\sigma_8$). The contours indicate 68.27 per cent and 95.45 per cent confidence levels. The result is for NGC at $z = 0.38$.

This paper has been typeset from a TEX/LATEX file prepared by the author.

Published by Oxford University Press on behalf of Royal Astronomical Society